

Alma Mater Studiorum - Università di Bologna

DOTTORATO DI RICERCA IN
INGEGNERIA ELETTRONICA, TELECOMUNICAZIONI E
TECNOLOGIE DELL'INFORMAZIONE

Ciclo 34

Settore Concorsuale: 09/F1 - CAMPI ELETTROMAGNETICI

Settore Scientifico Disciplinare: ING-INF/02 - CAMPI ELETTROMAGNETICI

WIRELESS POWER LINK DESIGN FOR BOTH HIGH-POWER INDUCTIVE
COUPLING AND SMART METASURFACES EXPLOITATION

Presentata da: Ghulam Murtaza

Coordinatore Dottorato

Aldo Romani

Supervisore

Alessandra Costanzo

Co-supervisore

Diego Masotti

Esame finale anno 2022

Index

Abstract..... 10

List of Abbreviations..... 12

Chapter 1: Wireless Power Transfer and SWIPT

1.0. Introduction 14

1.1. WPT Applications..... 16

1.2. Simultaneous Wireless Power and Information Transfer ...21

1.3. Trends and Standards in WPT..... 24

Chapter 2: Inductive WPT: The way forward

2.0. Introduction..... 26

2.1 Efficiency of Inductive WPT 26

2.2 Link Efficiency 27

2.2.1 Compensation Techniques 31

2.3.0 Inverter Efficiency 32

2.3.1 Soft Switching 34

2.3.2 Class E inverter 34

| | |
|----------------------------------|----|
| 2.3.3 Choice of the Switch | 36 |
|----------------------------------|----|

Chapter 3: Simultaneous Wireless Power and Information Transfer for Transport System

| | |
|--|----|
| 3.0. Introduction..... | 37 |
| 3.1 Design of the Coil | 38 |
| 3.2 Optimization of Class E inverter | 39 |
| 3.3 Analysis of the Losses | 42 |
| 3.4 Realistic Wireless Link Design..... | 44 |
| 3.5.0 Moving Towards SWIPT | 46 |
| 3.5.1 Design of Transmitter front-end (Printed Coil Antenna)... | 47 |
| 3.5.2 Description of the Problem | 49 |
| 3.5.3 Design of the Amplifier | 50 |
| 3.5.4 Results and discussion for Different Misalignments at d=200mm | 51 |
| 3.5.5 Isolation of the Power Coil from the Co-located sub- systems | 53 |

| | |
|--|----|
| 3.5.6 Efficiency of the System | 54 |
| 3.6 Driving Circuit | 55 |
| 3.7 Realization and Testing | 56 |
| 3.8 Conclusion and Future Prospect..... | 57 |
| Chapter 4: Intelligent Reflective surfaces | |
| 4.0 Introduction | 59 |
| 4.1 Globally Tuned metasurfaces | 60 |
| 4.2 Locally Tuned metasurfaces..... | 61 |
| 4.3 Applications of the Metasurfaces..... | 62 |
| 4.4 Intelligent Anomalous Reflector | 64 |
| 4.5 Working Principle | 65 |
| 4.6 Conclusion | 69 |
| Chapter 5: Design of Metasurface Based Polarization Converter and IRS | |
| 5.0 Introduction | 70 |
| 5.1 Working Principle..... | 70 |

| | |
|---|-----------|
| 5.2 Proposed Design of the Polarization Converter | 72 |
| 5.3 Results and Discussion | 75 |
| 5.4 Angular Stability of the Metasurface | 77 |
| 5.5 Reflection Angle Measurement | 78 |
| 5.6.0 Globally Tuned IRS..... | 81 |
| 5.6.1 Introduction to Proposed IRS..... | 81 |
| 5.6.2 Tunability and HfZrO | 82 |
| 5.6.3 Proposed Design of IRS..... | 84 |
| 5.6.4 Super Cell Configuration..... | 85 |
| 5.6.5 Interdigital Capacitor..... | 86 |
| 5.7 Conclusion and Future Work | 88 |
| Chapter 6: Summary of the Thesis | 89 |
| References | 92 |

Acknowledgement

It is indeed an honour for me to be a part of the DEI University of Bologna. I would like to extend my gratitude to Prof. Alessandra Costanzo and Prof. Diego Masotti who helped me throughout my PhD with great patience. Their supervision helped me improve myself continuously.

I would also like to thank my colleagues Dr Giacomo Paolini, Ms Francesca Benassi, Dr Mazen Shanawani and Mr Shobit Agarwal who helped me during my research period and were a great company to have in the lab. Without their support and help, things would have been more difficult.

There are some other people as well who has played equally important role in my life in Bologna and kept me motivated. I would like to thank Dr Usman Hadi and Mr Bilal Ahmed for their unparallel support and friendship.

Lastly, I would like to thank my family who was a great emotional support for me in the tough times of covid. They stood by me through thick and thin and extended all possible means of help they could have.

Abstract

Wireless power transfer has become extremely popular over the last decade because of its relevance in many applications. As future technologies are going to be autonomous under the umbrella of the Internet of things (IoT) we can expect WPT is the only way forward for the intelligent devices of the future. WPT has already found its place in many industrial and medical applications both in the near-field and far-field domains. The Impact of the WPT is going to further increase in many other applications. Therefore, this thesis is also an attempt to design and realize both near-field and far-field WPT solutions for different application scenarios.

A 27 MHz high frequency inductive wireless power link has been designed for transportation application. In order to maintain the efficiency consideration, the Class-E switching inverter has been designed to compensate for the efficiency loss because of the varying weak coupling between transmitter and receiver because of the movement of the Tx. A stepwise approach has been adopted in which only the power transmission has been considered initially and then a system of three coils was introduced with the prime focus on WPT. The other two coils are designed to fulfil the purpose of communication and testing, operating at frequencies different from the WPT coil. In addition to that, a trapping filter technique has also been adopted to ensure the EM isolation of the coils. The end product is a SWIPT system with an additional testing coil to be used in transportation scenarios.

In addition to this, a split ring resonator-based polarization converter has been designed. This converter can convert the TM to TE polarization and

vice versa with good efficiency and also over a wide frequency range. The SRR configuration has been adopted. The gap or cuts have been introduced in the adjacent sides of the square ring to make it a dual-polarization converter. It has been shown that this converter is also stable over a wide range of incident angles. In the end, a comparison between the performance of the proposed metasurface with other similar metasurfaces has been given.

In the far-field WPT link design, the meta element based intelligent surface has been designed to work in the reflection mode at 5 GHz. Initially, a study has been done successfully to lay the foundations of efficient beam steering. Traditionally, the response of each meta element is controlled by introducing computer-controlled ICs between the meta elements to have local control over the impedance of the surface. However, in this research activity, a different design methodology has been adopted by introducing interdigital capacitors (IDCs) instead of ICs and a thin layer of the HfZrO between substrate and meta elements whose response can be tuned and controlled with the applied voltage across HfZrO. This would allow designing an intelligent reflective surface suitable for many applications to steer the EM waves towards the desired direction.

The research activity provides a blend of near-field and far-field link analysis and optimization possibilities to be used in WPT applications.

List of Abbreviations

| Abbreviation | Explanation |
|---------------------|---|
| AI | Artificial Intelligence |
| AZ | Azimuth |
| BW | Bandwidth |
| CMOS | Complementary Metal–Oxide–Semiconductor |
| DC | Direct Current |
| DGS | Defected Ground Structure |
| EH | Energy Harvesting |
| EV | Electric Vehicles |
| EM | Electromagnetic |
| FCC | Federal Communications Commission |
| FM | Frequency-Modulated |
| GPS | Global Positioning System |
| HB | Harmonic Balance |
| HfZrO | Hafnium Zirconium Oxide |
| IC | Integrated Circuit |
| ICNIRP | International Commission on Non-Ionizing Radiation Protection |
| IRS | Intelligent Reflective Surface |
| ITU | International Telecommunication Unions |
| IPT | Inductive Power Transfer |
| IoT | Internet of Things |
| IDC | Inter Digitated Capacitor |

| | |
|-------|--|
| ISM | Industrial, Scientific and Medical |
| IMDs | Implanted Medical Devices |
| LOS | Line-of-Sight |
| MCU | Microcontroller Unit |
| MPR | Maximum Power Ratio |
| NLOS | Non-Line-of-Sight |
| PCR | Power Conversion Ratio |
| HEMT | High Electron Mobility Transistor |
| PAE | Power Added Efficiency |
| PA | Power Amplifier |
| PS | Phase Shifter |
| R&D | Research and Development |
| RF | Radiofrequency |
| RFID | Radiofrequency Identification |
| SAR | Specific Absorption Rate |
| SRR | Split Ring Resonator |
| TPA | Tuneable Perfect Absorber |
| UAVs | Unmanned Aerial Vehicles |
| WBG | Wide Band Gap |
| SWIPT | Simultaneous Wireless Information and Power Transfer |
| WSN | Wireless Sensor Network |

CHAPTER 1

Wireless Power Transfer and SWIPT

1.0 Introduction

Wireless power transfer is not a new subject but for a long time it was not being exploited to its full potential. The concept of the WPT was first given by the legendary scientist Nikola Tesla. The idea of WPT which was to become steppingstone for the new industrial revolution in 1906, did not attract much attention of the scientific community. However, 21st century is certainly going to see that revolution being realized.

Things have turned around dramatically since the last decade or so in the favour of WPT. WPT is increasingly in demand because of the increase in the use of the number of electronic devices in our daily life. These electronic devices are not just our mobile phones and tablets but now because of the commitments of the nations to environment friendly solutions, the number of electric vehicles (EVs) is also increasing. In addition to that, implanted medical devices (IMDs) and implanted identification chips are attracting a lot of scientific research. EVs and all other electronic devices need to be recharged using WPT techniques. As the fourth industrial revolution is in the making under the paradigm of IoT, WPT would play a key part in its realisation.

We can classify WPT in two basic categories depending upon the energy carrying waves.

1. EM waves
2. Sound waves

WPT using sound waves is a relatively new research area as compared to the WPT with EM field and it has found its application in the aviation industry. However, WPT using EM waves is much developed comparatively but it is still getting more and more attention especially in the context of IoT for the future. The last fifteen years have seen a gigantic leap in terms of number of research articles and number of patents published on this topic.

We can further classify EM field based WPT into different groups as shown in the Fig.1

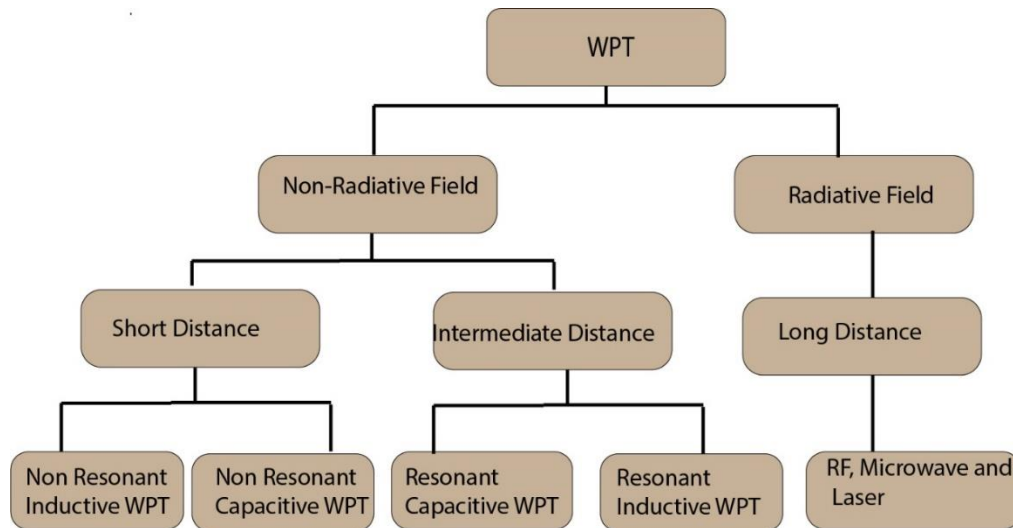


Figure 1 Classification of WPT systems

WPT systems are possible in both near-field and far-field regions. Both have their pros and cons associated with them. Near-field WPT is done at low frequency and with high efficiency while radiative WPT is done at a higher frequency, but the efficiency of the power transfer is very low in that case. Similarly, for the high-power considerations, low frequency near field systems is preferred. Near-field WPT is best suited for the short distances because of the reactive coupling between the transmitter and receiver while for the large distances far-field solutions are preferred.

1.1 WPT Applications

Wireless Power Transfer has been a hot topic for the last decade or so and it continues to be the topic of interest for many research groups. We can expect that the research in a large variety of the areas related to WPT will take place in future as well. It is most likely that we are going to see WPT systems all around us in the coming decades. Fig 2. Identifies currently exploited application areas for WPT.

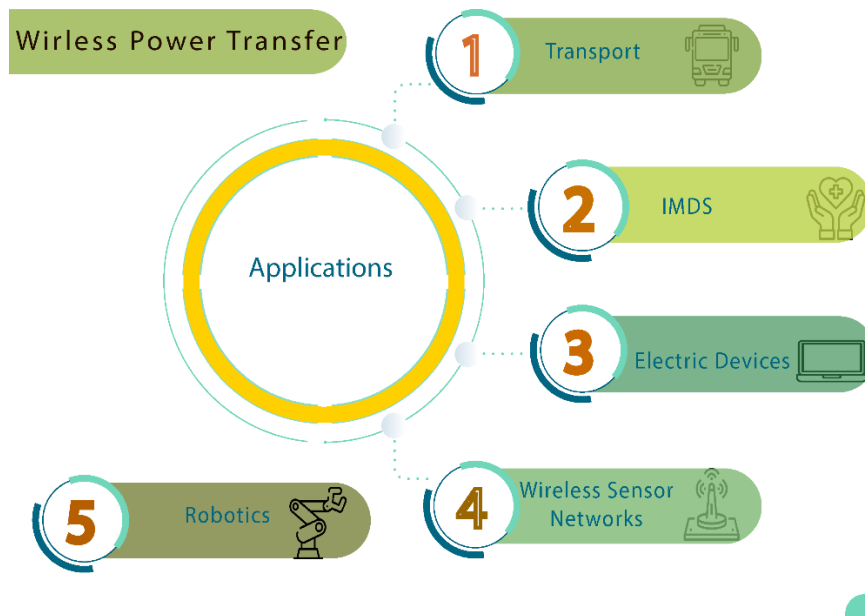


Figure 2 WPT Application Chart *¹

The implanted medical device is one such field which is drawing a lot of research interest of the scientific community. These implanted devices need power to operate. However, powering these devices with an electric cord is a dangerous proposition especially because of the infection risks

¹ Graphic sources are taken from flaticon and freePik.com

and such a solution cannot be pursued on a long-term basis. Therefore, a lot of the research is being carried out in that direction.

The resonant WPT systems are among the most popular systems for the biomedical implantable devices, one such approach is being discussed in [1] where an omnidirectional inductive WPT has been discussed.

Another omnidirectional approach has been reported by [2] where they have enforced WPT for IMDs using two different structures of the coils. In [3] a unified approach has been adopted to power several IMDs with different power requirements. Similarly, a multi-band low-cost inductive WPT approach has been proposed by [4] to power the implanted devices at different frequencies. IPT applications are founding their place as researchers are trying to cure brain related medical issues through IMDs. In that direction, a WPT system to provide low frequency electrical pulses to the nerve cells has been proposed in [5]. The experiment was performed on a rat. Another WPT link for brain implant has been proposed in [6] and this implant was made in the head of a pig. We can see that brain implanted WPT applications are still in their early stages as implants are only done on the animals so far, but we should expect that it will soon be available to cure and assist our sensitive brains. Near-field WPT systems are misalignment sensitive and in medical application this problem becomes particularly sensitive as the human body remain in motion and at different

pressures. To compensate for this effect [7] has presented a solution for the WPT IMDs. In addition to that [8] discusses a circularly polarized radiative near field solution used in IMDs for WPT purposes. Although the far-field IMDs solutions are not very common as compared to near-field solutions but [9] proposes a broadband WPT system which can be integrated with the pacemaker. There are many other research articles related to biomedical implants dealing with the endoscopy, Ocular devices and cardiac-related devices which are summarized in [10].

Electric vehicular WPT is also among the very hot topics these days. WPT for the EVs is done at the lower frequency as compared to the other applications. These high power WPT applications must be of good efficiency and for that, a zero-voltage switching (ZVS) based hybrid approach has been adopted to power the EVs [11]. An intelligent WPT system at 40 kHz frequency has been proposed in [12] for a moving vehicle which can also detect the presence of the vehicle. Localization of the electric vehicle is also possible by measuring the change of mutual inductance [13]. Another problem regarding the position of the EV is the misalignment between Tx and Rx. [14] presents a self-correcting mechanism to ensure the efficient transfer of power. Effects of misalignment can also be mitigated by controlling the turn-on point of the rectifier [15]. High power systems are preferred for their fast charging of

the EVs, but the power capability is limited by the power handling capability of the power devices and resonant elements, to overcome such an issue a four-channel 50kW powering system is proposed in [16] which is robust and efficiently handles high power at 85kHz operating frequency, a similar approach has also been adopted [17]. Another issue in every IPT application is the efficiency of the link itself. Efficiency of the link plays a very important role in the overall efficiency of the WPT systems therefore a new 2-layer coil design is proposed in [18] which improves the magnetic flux as compared to the unlaminated coils. The efficiency of the WPT system can also be improved by exploiting compensation topology like double-sided tuneable lumped elements one such technique has been used in [19] which provides the load independent and a stable WPT system. Shielding of the WPT system for EV is another important parameter in improving the link efficiency and its performance, [20] utilizes ferrite plate and annular aluminium plate as shielding material to reduce eddy currents and to improve the efficiency. Research is being carried out to push the performance of the WPT systems further by introducing new and unconventional materials like High-Saturation Nanocrystalline Cores and Carbon Nanotube Fibres (to be used instead of copper wires) [21,22] and with the availability of the wide bandgap switching devices [23], industry of WPT for the EVs is going to flourish rapidly.

Wireless sensor networks (WSNs) have also benefited from WPT. WSNs are important for monitoring, processing and sending data from one node to another. In the context of smart cities, they are going to play an important role. All these sensors have batteries connected which are to be changed periodically once depleted. In the case of a distant sensor, this is not feasible. Therefore, to cope with this energy bottleneck, far field WPT is going to play an important role. So, in the future, a true smart city model would only be possible only if it has WSNs which are WPT enabled. [24] proposes a power beacons model which are nothing but RF energy sources to satisfy the energy needs of WSNs. Another approach can be of a moving WPT source which, depending upon the priority set according to the importance of the node in a network, should power WSNs as discussed in [25]. The mutual powering mechanism is also an important factor for WSNs, [26] proposes a unique solution of self-energizing WSNs where each sensor node has been enabled to power other sensor nodes wirelessly. A more comprehensive approach is being adopted by [27] implementing both near-field, far-field WPT mechanisms for different power requirements of the WSNs. [28] reports that instead of a separate WPT system WSNs can be provided with power, using a SWIPT approach which uses frequency modulated signal. Moreover, beam scanning technique is also a solution to cover a specific area of WSNs, [29] exploits the same idea

of using a directive leaky-wave antenna operating from 2.4 GHz to 2.5 GHz for WPT.

Moreover, a lot of industrial and other commercial applications are being automated and manpower is being replaced by the robots. These robots are power-hungry entities in any environment and their power requirements may vary according to the nature of the task. Enabling WPT can provide a great deal of flexibility to the robots and can avoid potential hazards i.e., electric shocks. As is the case in the other fields of applications, robotics is also benefitting from the WPT technology. [30] proposes an omnidirectional WPT model for the logistic robot. WPT is particularly important in the case of robotic swarms and [31] presents one such scenario where each robot can exchange energy with the other.

1.2 Simultaneous Wireless Power and Information Transfer

We are stepping closer to the 4th-industrial revolution, whose foundations are laid by the IoT, where number of smart devices would be working in harmony. This revolution is pushing from smart-homes to autonomous smart-cities. With the increase of number of devices, the need will arise to power these devices smartly and for that an intelligent WPT network is a prerequisite.

SWIPT offers a very logical solution to address power issues for the smart cities.

SWIPT systems can be classified into two broad categories depending upon the modulation schemes used.

- In band modulation: Where the power carrier signal is modulated to transmit the information [32]
- Out band modulation: Where the secondary band is used to transmit information

In band modulation schemes do not offer a large data rate as the later can provide [33]. An application where a large power and data is to be transferred out-band solutions are more suitable and possible choices can be NFC and Bluetooth enabled WPT systems. In the following paragraph trends followed by the research communities towards the SWIPT are presented to see the prospects of SWIPT.

In almost all the applications, discussed earlier, SWIPT has its relevance. A multi-transmitter and multi-receiver SWIPT system is proposed in [34] exploiting in-band modulation at 6.78 MHz and a relay resonant network has been adopted to enhance the efficiency of the overall system. [35] proposes a resonant network assisted with an automatic tuning network which ensures resonance conditions even if the switching frequency is not the same as the resonant frequency, making it possible to adopt frequency shift keying (FSK) for the information transfer without degrading the power of the system. A slightly different SWIPT technique has been adopted by [36] where power is transmitted on a large unmodulated signal and a small signal is being used for communication. A multitone frequency shift SWIPT system is proposed in [37] where modulation is achieved by changing the number of tones which makes an overall system more efficient as the demodulation is done by sensing peak to average power

ratio. A defected ground structure (DGS) and special planar inductor geometry have been adopted in [38] for out-band communication-based SWIPT systems at 50 MHz and 100 MHz. [39] discusses the interoperability of WPT and NFC networks and presents an equivalent circuit which can be used to better optimize the SWIPT systems. These SWIPT systems can also be utilized as wearable devices in health monitoring scenarios one such application is being discussed for monitoring the breathing pattern of hospitalized persons in [40]. Similarly, another far-field SWIPT system is also being exploited in [41] for biomedical implants working at 915 MHz and 1470 MHz for communication and WPT respectively. [42] deals with the SWIPT system with an emphasis on the improvement of the uplink communications by introducing a passive circuit to produce strong pulsed magnetic field. In addition to that, SWIPT system meant for the contact lenses to detect biomarker of the different disease have been proposed where the inductive WPT in the ISM band is done and data is transferred from the sensor. There can also be detection SWIPT system as discussed in [43], it represents an interesting application utilizing NFC /WPT based system which can detect the freshness of the beverages at 10 MHz frequency. SWIPT systems are all about the intelligent solutions, [44] adopts an envelope-detector based low power demodulation scheme to increase the power conversion efficiency. Similarly, [45] proposes an antenna array to improve SWIPT systems and deliver benefits when used in a Wireless Sensor Network (WSN) architecture. The proposed 3D antenna array is made up of eight 5.65 GHz antenna elements.

The quantum of applications discussed above establishes the importance of WPT systems. There can be numerous other applications as well which are going to exploit new trends in WPT in the future.

1.3 Trends and Standards in WPT

With the increase in demand for the WPT systems, many companies both small and large sprung up to fill up the vacuum to provide reliable WPT solutions for the charging of all kinds of electronic devices ranging from home appliances to EVs. When it comes to electronic devices and electric vehicles near field WPT is more famous than the far-field WPT. Therefore, the need for some standards and set parameters is natural. However, these standards are not unified and there can be a difference in that approach depending upon the region.

Predicting the exponential increase of the WPT systems in the coming year, Wireless Power Consortium (WPC) was established in 2008 to provide a common platform for the emerging companies which will also help to set the standards for WPT systems. There are several industry standards set for WPT. Some of them are already well established, while others are under consideration. While considering near field WPT, two standards are in the forefront namely Qi (chee) and Airfuel. Qi standard is the most established and commercially utilized standard which works at 100 to 300 kHz frequency range for delivering power between 5W to 15W. Several companies like Apple, Samsung and Huawei are making Qi enabled smartphones. Other standards like the one set by Airfuel are operating at 6.78MHz. Both standards are for the near-field WPT but there is a fundamental difference between these two standards as well. In the Qi standard, the information is encoded on the power signal itself, while Airfuel uses a secondary signal (i.e. Bluetooth standards) for that purpose. There are other frequency bands like around 13.56 MHz and 27.1 MHz used for inductive WPT in North America (i.e. FCC and Canada).

In the case of Europe, there is a joint effort being done under Cost Action IC1301 which will help developing a unified approach. Unlike America where there are two different approaches to deal with a device being a radio device, but in Europe under the Radio Equipment Directive (RED 2014) any device meant for WPT and transmits data is a radio device. There are a number of documents available at the European Telecommunication standards institute (ETSI), which govern the standards and frequency allocation for WPT. EN 300 330 is one such document which allows the use of 6.78MHz, 13.5 MHz and 27 MHz frequencies to be used for the inductive applications. However, the band of frequencies around 27MHz is used in the railways-based application systems. Almost all IPT systems fall under the 30MHz frequency limit in Europe, to be used in generic applications which are governed by REC 70-03/ EU 2019/1345.

In case of the WPT systems designed for the high-power applications, for example, charging of the electric vehicles, low frequencies are being recommended by International Telecommunication Unions. These frequencies fall into different bands between 20kHz and 90kHz.

As the research will grow the standards and protocols are going to be more generalized and homogenized, but we can expect that, with the field of WPT reaching maturity by small endeavours undertaken by the scientific and research community worldwide.

CHAPTER 2

Inductive WPT: The Way Forward

2.0 Introduction

Inductive WPT is by far the most exploited method largely because of the better efficiency and capabilities of this method to transfer high power. In many applications where power transfer is needed for the short ranges, IPT becomes the default choice, for example, charging of the electronic devices, home appliances and charging of electric vehicles, etc. As power transfer in IPT is because of the magnetic fields IMDs opt this technology because of the polar nature of the water molecules in the human body and presence of strong electric field can cause some unwanted problems.

However, WPT through inductive coils is not a straightforward problem. There are a number of issues to be considered for an efficient IPT system. In the following sections, a detailed overview of different aspects of IPT will be discussed.

2.1 Efficiency of Inductive WPT

In every WPT system efficiency is the most important parameter to be taken care of. A simplified perspective of the overall efficiency of the IPT is presented in Fig 3. In the following sections, a detailed overview of different aspects of IPT will be discussed. We can divide it into three broader categories.

- Link Efficiency or RF to RF Efficiency
- The efficiency of the Amplifier or DC to RF Efficiency
- Rectification Efficiency or RF to DC

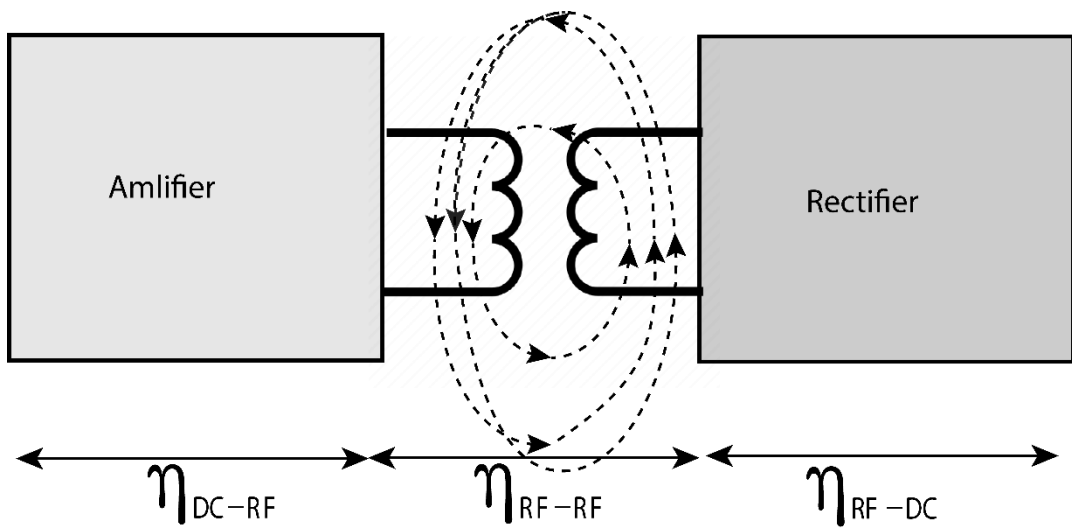


Figure 3 Efficiency Description of a WPT System

2.2 Link Efficiency

The link efficiency depends upon various factors. It depends upon the size of the coil, inter coils distance and alignment between Tx and Rx. The basic principle of the inductive link is based on Amperes law and Faraday's law. According to which a time-varying current in a primary coil produces a time-varying magnetic field and when present in the proximity of secondary coil, change of magnetic flux induces an emf in the secondary coil. Basically, the IPT link works on the same principle as a transformer but in the case of transformer, we use a metallic core to link the flux of a primary coil to the secondary coil. Because of the presence of the core, the coupling between the coils is very strong. However, we must remove the core in WPT scenarios to achieve flexibility as in many IPT applications Tx and Rx cannot be fixed. An IPT link without the core is known as the weakly coupled transformer. Weak coupling leads to the reduction in the magnetic flux. However, loose coupling does not mean that IPT is not

efficient. There are many design parameters and technique which can improve the IPT efficiency.

The presence of the mutual coupling between the coils makes the mathematical analysis of the link complicated. Therefore, to better understand this discussion there are many models present in the literature to derive the overall efficiency of the link [46].

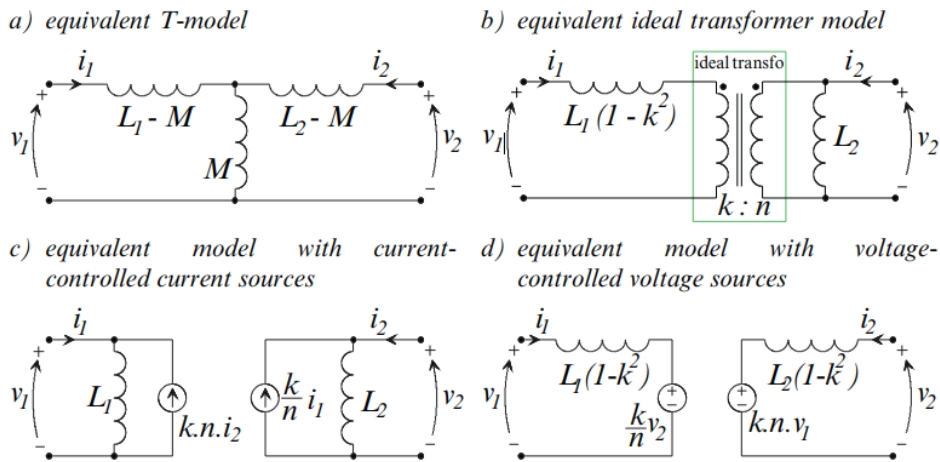


Figure 4 *Equivalent Circuit Models for the coupled link [46]*

The equivalent T-model separates the noncoupled part of the inductances from the mutual inductance. These noncoupled inductances are present as leakage inductance. It models the mutual inductance M as a self-inductance, with the same value. The ideal transformer method works on the same method of splitting inductance to reduce the link for the circuit analysis. Similarly, there are other two circuit level descriptions of the link which use voltage and current sources to model the effect of mutual inductance of the link as shown in Fig4.

Similarly, there are other methods which model the inductive link as a two-port network and can evaluate the efficiency [47].

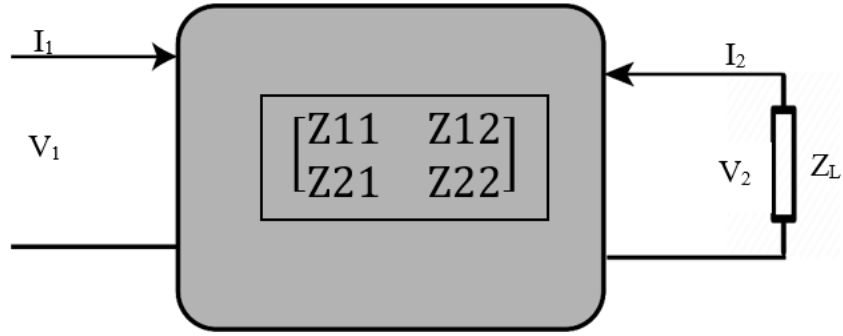


Figure 5 Two port network representation of the link

Two port voltage equations can be written as

$$V_1 = Z_{11}I_1 + Z_{12}I_2 \quad (1)$$

$$V_2 = Z_{21}I_1 + Z_{22}I_2 \quad (2)$$

and V_1 and V_2 are under the following assumptions.

$$V_2 = -Z_L I_2 \quad (3)$$

$$V_1 = Z_s I_1 \quad (4)$$

$$I_2 = \frac{-Z_{21} I_1}{Z_{22} + Z_L} \quad (5)$$

Putting Eq.5 in Eq.1, input impedance of the 2 port-network can be calculated as

$$Z_{in} = Z_{11} - \frac{Z_{21} Z_{12}}{Z_{22} + Z_L} \quad (6)$$

Similarly,

$$Z_{out} = Z_{22} - \frac{Z_{21} Z_{12}}{Z_{11} + Z_s} \quad (7)$$

From the above equations, we can calculate link efficiency as a ratio of output power to the input power of the network as,

$$\eta_{\text{Link}} = \frac{P_o}{P_i} \quad (8)$$

Considering, $Z_{12} = Z_{21} = j\omega M$

$$\eta_{\text{link}} = \left| \frac{z_{12}}{Z_L + Z_{22}} \right|^2 \frac{R_L}{R_1 + \frac{\omega^2 M_{12}^2 (R_2 + R_L)}{(R_L + R_2)^2 + (X_L + X_2)^2}} \quad (9)$$

Where R_L , R_1 and R_2 are the real part of the impedances associated with load, primary coil or transmitter, and receiver respectively. In order to see the dependence of efficiency on the coupling, the Eq.9 is often presented in terms of Q-factor and coupling coefficient. Q-factor of a coil is defined as,

$$Q_c = \frac{\omega L_c}{R_c} \quad (10)$$

The maximum efficiency of the system is dependent on the optimum load.

The optimum load condition can be achieved by differentiating Eq.9 with respect to R_L and X_L .

In [47] the $Z_{L\text{opt}}$ comes out to be

$$Z_{L\text{opt}} = R_L \sqrt{1 + k^2 Q_1 Q_2} - j\omega L_2 \quad (11)$$

Substituting Eq. 10 and Eq.11 in Eq. 9 gives the max efficiency.

$$\eta_{\text{max}} = \frac{K^2 Q_1 Q_2}{(1 + \sqrt{1 + K^2 Q_1 Q_2})^2} \quad (12)$$

Eq.12 shows that the efficiency of the link does not depend solely on the coupling between the coils. The efficiency of the coil also depends upon the Q-factors of the coil. However, there are techniques available in the literature to further increase the efficiency under resonance. These techniques are known as compensation technique.

2.2.1 Compensation Techniques

The compensation technique is utilized to eliminate the leakage inductance effect and to ensure the resonance. In case of inductive WPT, capacitive compensation is very common. There can be four possible combinations for capacitive compensation on transmitter and receiver, e.g., SS compensation means series capacitor on both Tx and Rx side. [48] provides a comparison of these compensation techniques.

The efficiency of the compensated link increases significantly as can be seen in Fig.6, where the effect of compensation of the secondary coil can be seen.

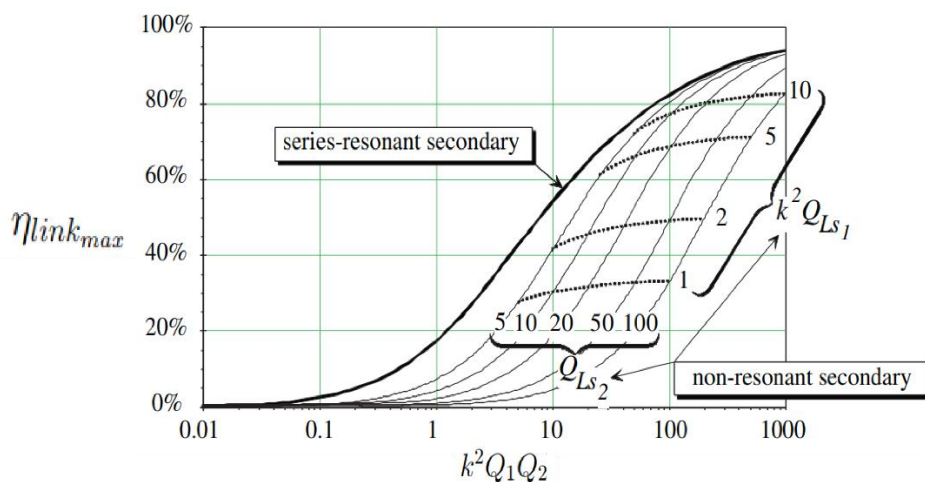


Figure 6 Graphical representation of the efficiency of compensated and uncompensated coils [46]

In summary, we can design a good inductive link by ensuring good quality factor. One of the ways is to increase the number of turns which increases the Q. In addition to this, we can move towards higher operating frequency which in turn increases the Q.

2.3.0 Inverter Efficiency

The second most important part in the design of IPT system is the RF power amplifier. While talking about the power amplifier there are two most important parameters for the choice of an amplifier. As we move from a linear to nonlinear amplifier, efficiency of the power unit increases, but the voltages and currents at the output stages are no more sinusoids.

Based on the operation of the transistor we can classify them into two categories.

- Transistor working in active or pinch off region
- Transistor, working as a switch

In the following table, a comparison of the performances of different power amplifiers has been presented.

Table 1 Comparison of the efficiency and Conduction angle of PAs

| PA | EFFICIENCY | CONDUCTION ANGLE |
|----------|------------|----------------------|
| CLASS A | 50% | 360 |
| CLASS B | 78.5% | 180 |
| CLASS AB | 50-78% | $180 < \theta < 360$ |
| CLASS C | 90% | $\theta < 90$ |
| CLASS D | 90% | Switching |
| CLASS E | 90% | Switching |
| CLASS F | >90% [49] | Switching |

Depending upon the application, the choice of the PA may vary. In any PA, the most important role is played by the switching losses and in case of IPT, which is already suffering from the weak coupling of the coils, the choice of PA becomes even more important. Therefore, all PAs which are based on the conduction of the transistor are not suitable. Which leads us to the choice of switching PA.

Class D amplifiers are working in the bridge configuration which means more losses as compared to single transistor configurations. Therefore, most IPT opt for Class E, Class F or other similar hybrid switching power amplifiers.

Class E and Class F inverters are based on the principle of waveform engineering done using an impedance network connected at the output stage of the switch.

These inverters can provide very high efficiency because of the zero voltage and zero derivative switching conditions imposed by the careful selection and optimization of the impedance network.

2.3.1 Soft-Switching

Zero voltage, and zero derivative switching is also known as soft switching. Which means that the switch turns on at 0 voltage making the product of current and voltage zero to ensure a zero-power loss in the switch.

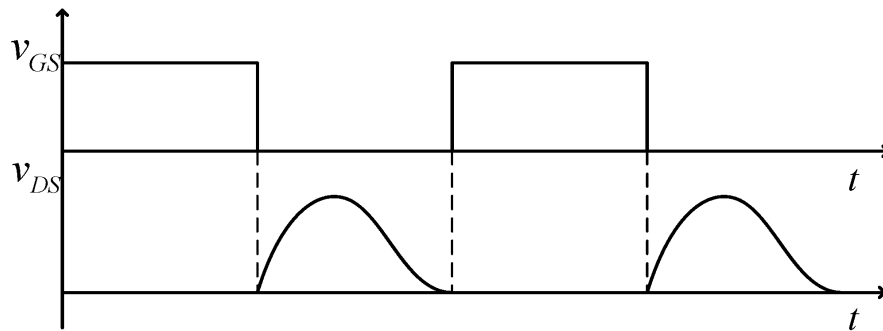


Figure 7 Switching Waveform at gate and Drain Voltage

Mathematically, we can represent it as

| | |
|----------------------|------------|
| $V_s(\omega t) = 0.$ | ZVS |
|----------------------|------------|

| | |
|---|------------|
| $\frac{dV_s(\omega t)}{d\omega t} = 0.$ | ZDS |
|---|------------|

To impose these conditions, the careful selections of the impedance must be insured.

2.3.2 Class E inverter

Class E inverter can provide high efficiency at high frequencies as well. The best performance of the class E can only be achieved at optimum load.

Fig.8 presents the basic topology of the Class E inverter.

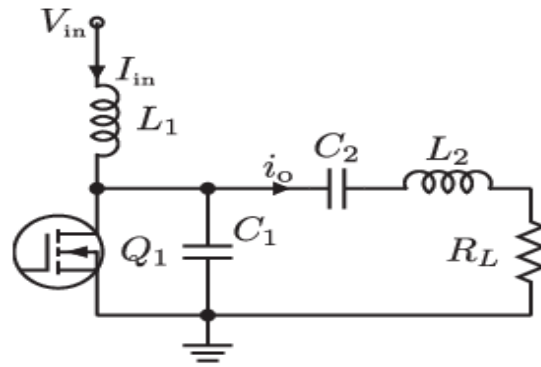


Figure 8 *Class E Inverter*

Choke inductor provides DC and blocks the AC ripples. The value of the Choke inductance is usually kept high. Capacitor placed in parallel with switch provides a short circuit path for the higher harmonics generated by the switching of the transistor. C_2 and L_2 are at resonance to provide a sinusoidal current through the load. The resonance frequency is kept the same as the switching frequency.

If biased properly, the switching losses can be reduced significantly as show in the Fig. 9 where ZVS and ZDS properties are being observed.

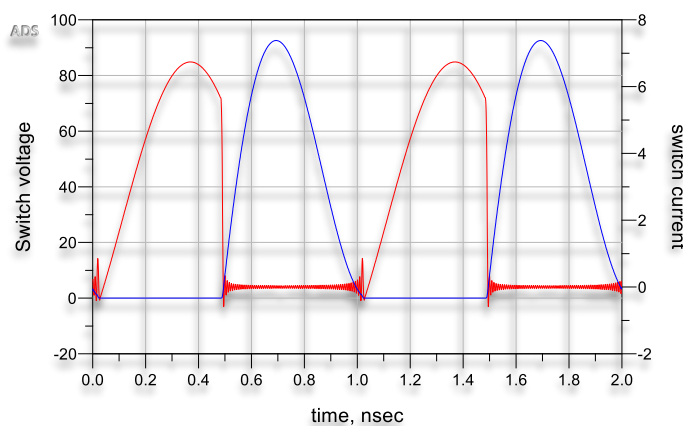


Figure 9 *Switch voltage and current waveform*

Class E inverter is known for its load independent quality as well [50]. Which makes it suitable for IPT applications where coupling is not constant.

2.3.3 Choice of the Switch

Losses in the switch are directly proportional to the switching frequency. Therefore, it is extremely important to choose a device which can perform efficient switching at higher frequency.

The wide bandgap (WBG) devices are very efficient at high frequency. There are two devices: Gallium Nitride (GaN) [51] and Silicon Carbide (SiC) [52] which have WBG property.

GaN can tolerate relatively high voltages and high maximum current due to high carrier density and high electron mobility. which makes it an ideal candidate for the high frequency high power application. GaN devices can also withstand higher temperatures.

Its ability to withstand high voltages is particularly suitable for the switching amplifiers to provide a constant power by reducing the current flowing through the impedance network. Which is because in such amplifiers we can control current by scaling impedances without changing the voltage across switch.

In the next chapter design of a SWIPT system will be presented based on the near field IPT based on the design and theoretical discussion done in this chapter.

CHAPTER 3

SWIPT for Transport System

This chapter is based on the following articles:

G. Murtaza, M. Shanawani, D. Masotti and A. Costanzo, "Optimization of a 27 MHz Wireless Power Transmitter for Unknown Receiver," 2020 XXXIIIrd General Assembly and Scientific Symposium of the International Union of Radio Science, 2020, pp. 1-4, doi: 10.23919/URSIGASS49373.2020.9232315.

G. Murtaza, M. SHANAWANI, D. MASOTTI, A. COSTANZO "Design of a SWIPT system with special consideration to the near-field WPT at 27MHz" in URSI radio science journal, vol. 2 ,2020

D. MASOTTI, M. SHANAWANI, G. MURTAZA, G. PAOLINI and A. COSTANZO, "RF Systems Design for Simultaneous Wireless Information and Power Transfer (SWIPT) in Automation and Transportation," in IEEE Journal of Microwaves, vol. 1, no. 1, pp. 164-175, Jan. 2021, doi: 10.1109/JMW.2020.3034661.

3.0 Introduction

This chapter will include the design of a SWIPT system for transportation applications. A 27MHz transmitter has been under consideration for the power transfer purposes, to include the transfer of the information for out-band modulation scheme, two independent transmitters working at 4MHz and 6MHz are introduced. 4 MHz transmitter is for the communication purposes and 6MHz coil is to transfer string of zeros to test the presence of Tx and Rx. A stepwise approach has been adopted to build the SWIPT system with the power amplifying section. The focus of the transmitter would be to design an efficient near field SWIPT system with more consideration to the power transferring section. Various aspects, as discussed in the previous chapters, regarding IPT, like the design of the coil, inverter design and mutual interference of the coils, have been considered and addressed.

3.1 Design of the Coil

As discussed previously, near-field inductive link for WPT works on the principle of weakly coupled transformer without a core. Hence reduction in the coupling can reduce the power coupling ability of the link. In that regards to improve the coupling, the improvement in the Q-factor of the coils is necessary. Eq.12 can also be written as

$$\eta_{opt} = (kQ)^2 / (1 + \sqrt{1 + (kQ)^2})^2 \quad (3.1)$$

Where k is the coupling coefficient and $Q = 2\pi fL/R$

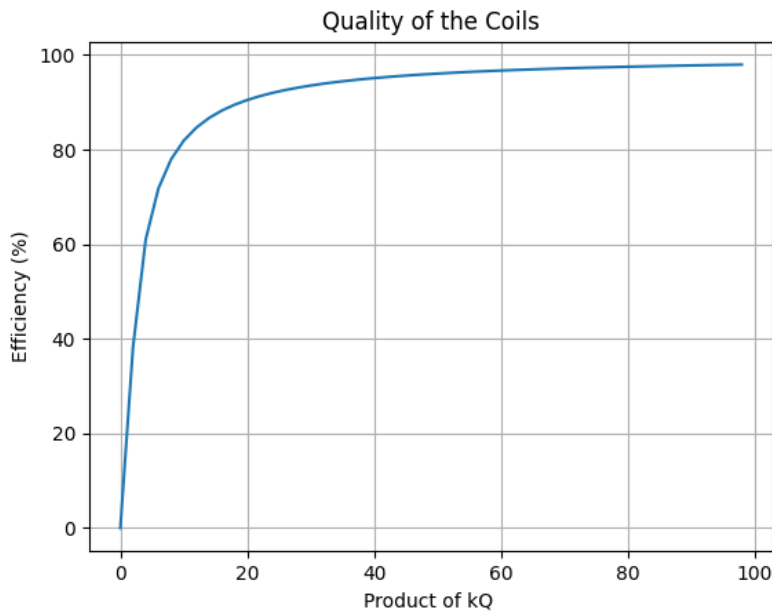


Figure 10 Efficiency Vs product of kQ

As it can be noted from Fig.10 that efficiency of the two-coil link is more than 80% when product of kQ is greater than 40.

Coupling factor of the coil is dependent on the distance and alignment of the Tx and Rx coil and in many applications, we don't have much control over k. Therefore, to increase the quality factor of the coil, we must increase

the inductance of the coil or must reduce the losses in the coil. However, these two parameters are inversely related which leaves one last option of increasing the operational frequency. Therefore, 27MHz operating frequency has been adopted to ensure the higher kQ , for the purpose of power transfer.

Initially, only power coil has been introduced on the Tx side and a link has been established by creating a generic Rx. Dimension of the coil is given in Fig.11.

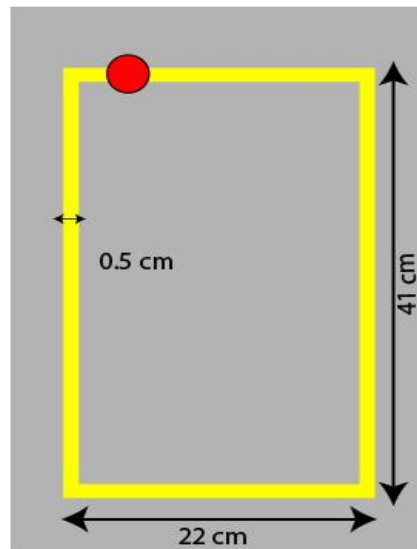


Figure 11 *Power Transmitter Coil*

3.2 Optimization of Class E Inverter

The Class E inverter has been adopted to power the Tx coil. Efficiency of the Class E can be maximized for an optimum load [53]. One can adopt matching techniques to achieve optimum load condition. Therefore, to ensure that power transfer is efficient, a matching circuit has been introduced before the Tx coil as shown in Fig.12.

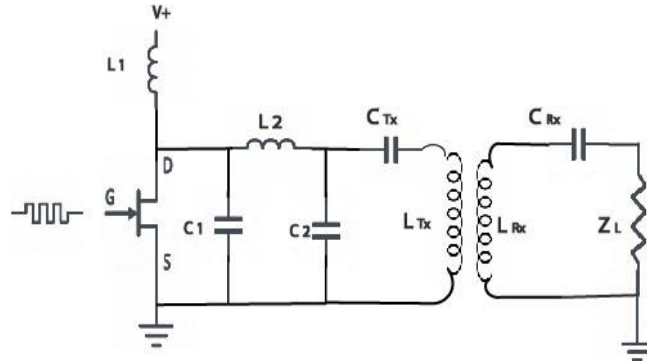


Figure 12 IPT with Class E

The shunt capacitor C_1 is responsible for the shaping of the switch voltage, and it also filters out the higher harmonics. Capacitor C_1 is also important to take into account the drain to source capacitance value of the Switch. The inverter output matching network consists of a shunt capacitance (C_2) and a series inductance (L_2) to drive the inverter under optimum condition for 120Ω load at the receiver side. L_1 is an $80\mu\text{H}$ choke used to provide constant current and stop any ac ripples going to the 8.5V voltage source connected at the drain.

50 % duty cycle of the switching waveform, driving the gate of the GaN device (GS66508b), has been chosen and the switching frequency is kept 27MHz with amplitude of the driving pulses varying between 0V - 5V . The duty cycle plays an important role and impacts output voltage of the switch. Therefore, this becomes an additional design parameter to be considered at the input. The 50% duty cycle here adopted is suggested in [53], because of the higher power output capability.

As a first trial to test the GaN device, a theoretically proposed T network has been chosen to represent the inductive link between transmitter and receiver as shown in the Fig.13.

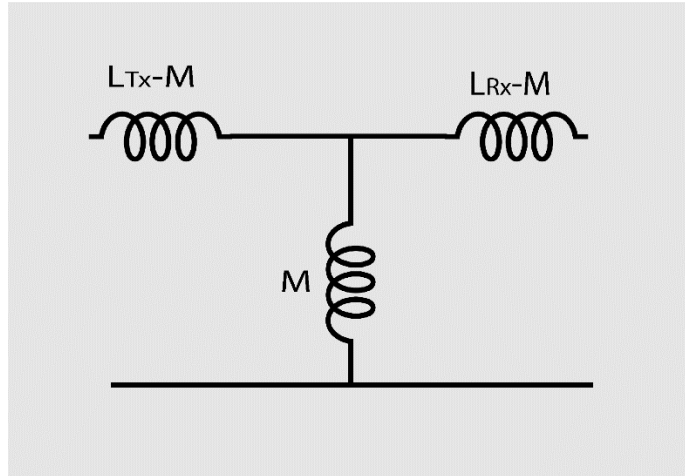


Figure 13 *T model representation of the link*

L_{Tx} represents the inductance of the transmitting coil and is chosen equal to $1 \mu\text{H}$, whereas L_{Rx} is the unknown inductance of the receiving coil, considered equal to 500 nH . M equal to 70 nH is the mutual inductance, evaluated in order to have a 0.1 coupling coefficient (k).

A nonlinear optimization with C_1 , C_2 and L_2 as design parameters is carried out.

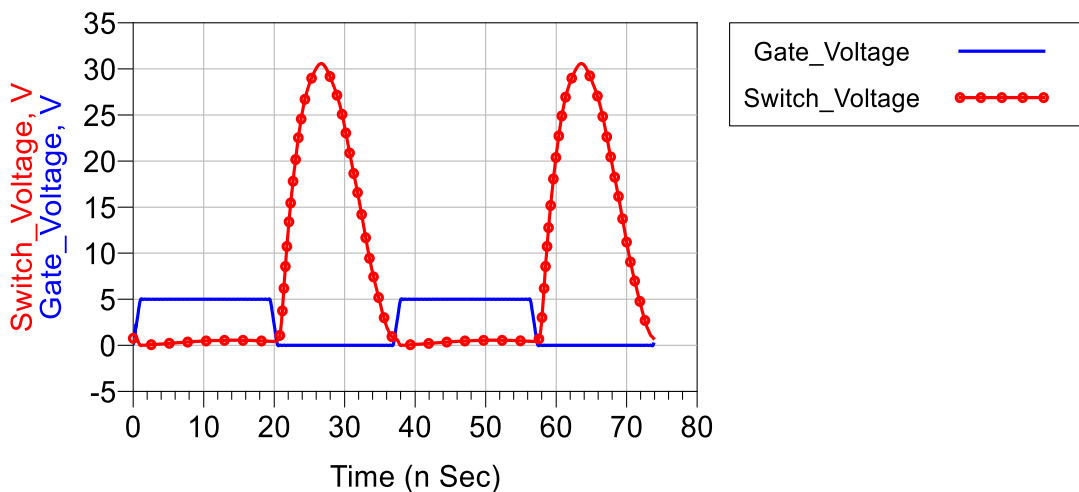


Figure 14 *Comparison of the Gate Voltage and Drain Voltage*

Fig. 14 shows the output drain voltage of the switch obtained for optimized Values $C_1 \approx 180 \text{ pF}$, $C_2 \approx 20 \text{ pF}$, $L_2 = 10 \text{ nH}$: it can be seen that the voltage

across the switch is in the optimum operating conditions providing zero voltage and zero derivative conditions. Similarly, Fig.15 shows the current through the load connected at Rx side of the T-network.

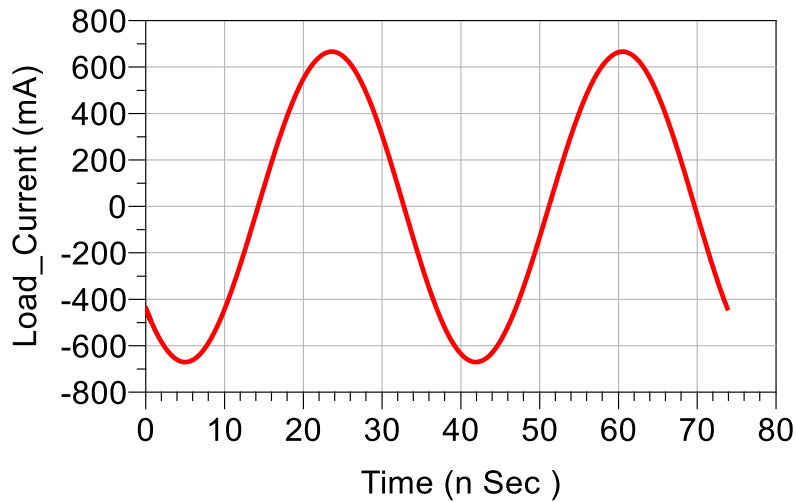


Figure 15 *Current through R_L*

Fig.15 validates the higher harmonic suppression and overall power added efficiency of the system, in this case, is 78 %.

3.3 Analysis of the Losses

There are many parameters to be considered for the efficient IPT including coil design, switching losses and variation of the loading conditions. To have an Idea of these losses and their effects, different losses have been introduced in the simulation.

A comparison between the ideal switch and GaN (GS66508b) switch has been made. When an ideal switch is considered, the class E switching amplifier has the ability to deliver power with more than 90% of efficiency. Fig.16 gives us a good idea of the losses because of the GaN switch and its comparison with the Ideal switch.

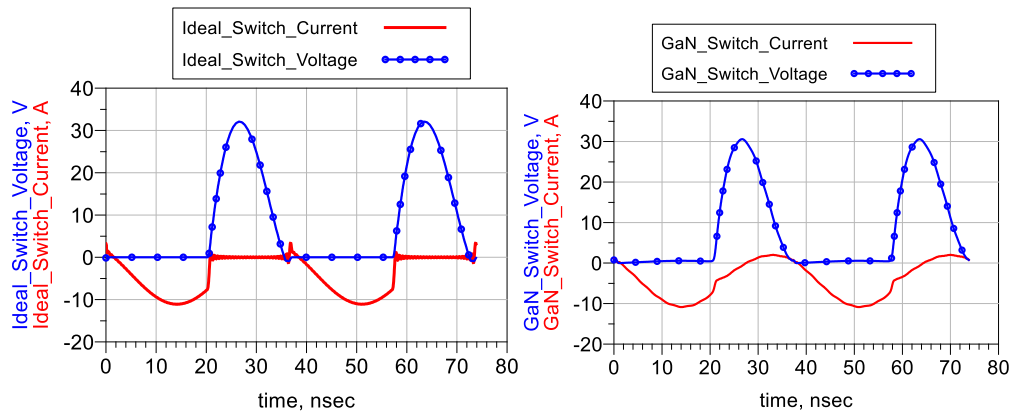


Figure 16 Comparison of the ideal and GaN switch

In Fig. 16, where the current and voltage waveforms of an ideal switch are reported, it can be seen that the product of current through the ideal switch and the voltage across it, is almost zero at every instant, thus leading to very low power losses in this case. However, in the case of the GaN (GS66508b) switch, it can be observed that the product of current and voltage is not always zero and, as a consequence, the efficiency is reduced to 78%, in our case.

Secondly, the losses introduced by the transmitter coil itself play a very important role in determining Q-factor of the coil as well as in determining the efficiency of the coil.

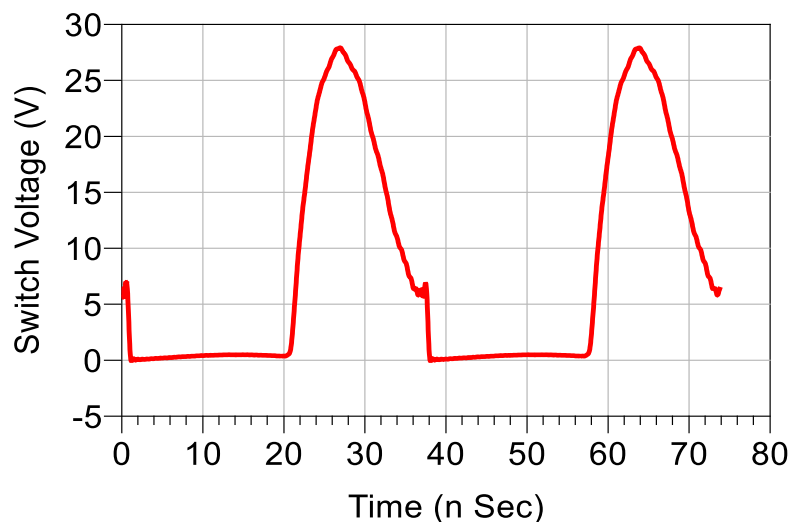


Figure 17 Switch Voltage in case of lossy Transmitter

When losses of coil are introduced in a tightly coupled conditions the efficiency of the system reduced to 61% which was a significant loss. This loss is because of the unsatisfied soft-switching conditions as shown in the Fig 17.

Similarly, variation of the load between 100Ω to 140Ω has been done as shown in Fig 18. We can see that, as the load varies, there is a small degradation in the shape of the switch voltage and the variation in current is very small as well: the corresponding efficiency values ranges from 75% to 80%.

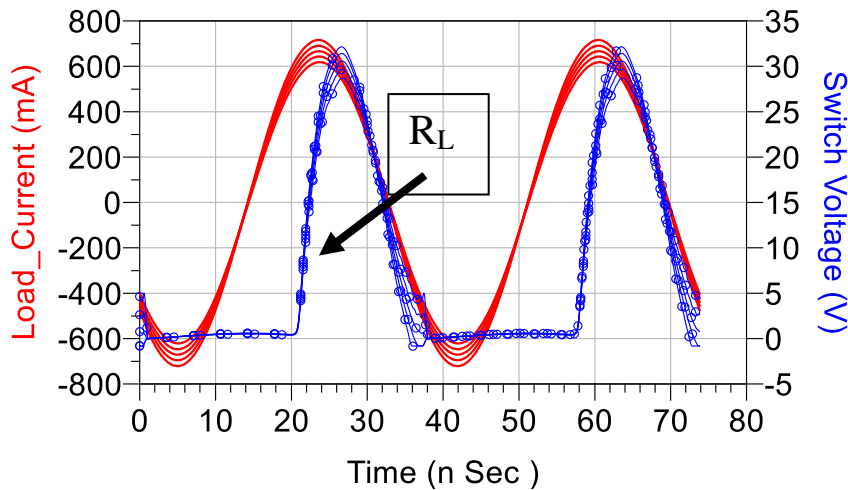


Figure 18 Effect of load variation on switch voltage and load current

3.4 Realistic Wireless Link Design

A realistic link between the transmitter coil and a generic receiver has been designed and electromagnetically simulated. Fig. 19 shows the link under examination, where both the coils have a protective aluminum plate behind them. The distance between the transmitter and the receiver is 22cm.

CST Microwave Studio is used for the full-wave simulation. Frequency domain solver is used as it is best suited for the narrowband resonant structures.

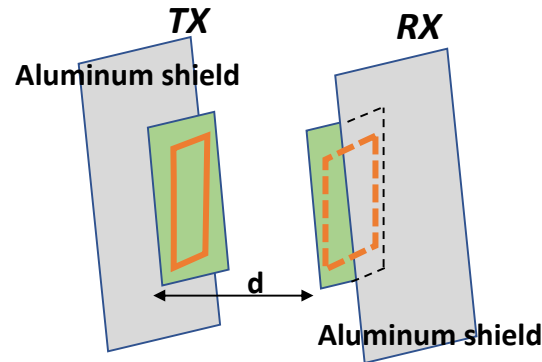


Figure 19 IPT link description

A generic receiver has been used to establish a wireless link between Tx and Rx. Fig.19 makes a two-port network schematic where the link can effectively be represented by its S-parameters. Therefore, in order to introduce the effect of real links S parameters, generated by the full-wave simulations, have been used to account for the wireless link instead of the T model which does not include the parasitic effect. As the distance is very large the mutual coupling is weak which will result in less power delivered to the load. Zero voltage switching is slightly disturbed but 2W of power is being received in this case. Current through load and switch voltage have been shown in Fig.20, indicating that with the introduction of the real link parameter, the proposed optimized topology is still able to function properly.

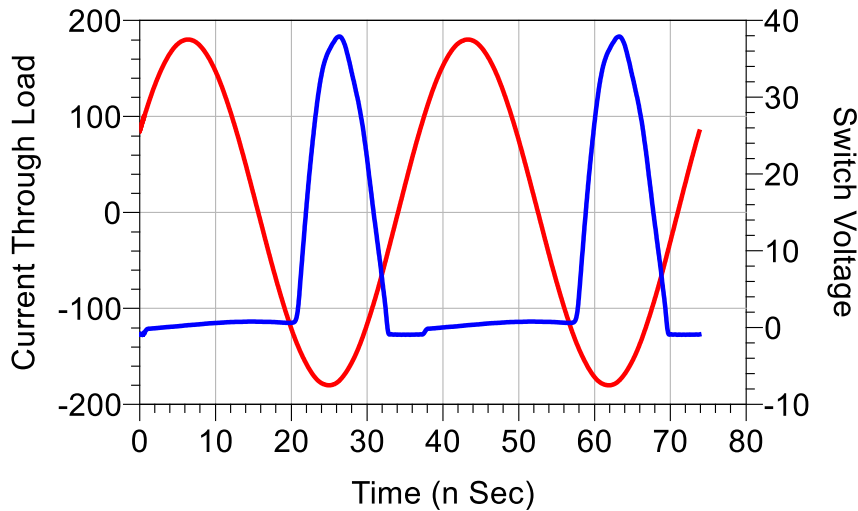


Figure 20 ZVS and Current through load in the presence of real link

The above study gives us the basic foundation to understand the IPT related shortcomings to be avoided in forthcoming SWIPT system, which will be discussed in the next section.

3.5.0 Moving Towards SWIPT

SWIPT is an integrated system where the transmission of the power and information are considered simultaneously. One such SWIPT system is under consideration for the transport application. The proposed SWIPT system is to be integrated on vehicles. Such applications demand a robust system which should be able to provide power and transmit information signal under harsh weather environment as well. One such example can be of a railway system where SWIPT systems are installed on board to communicate with a receiver present in the railway tracks. Hence, an efficient and robust system is the only solution which should be able to withstand such conditions.

IPT enabled SWIPT systems are near field systems which usually use two coils dedicated for power and information, other solution is [54] where coils working at low frequencies are used to transfer power and, for the

communication purposes, it adopted Bluetooth technology to avoid interference. Interference is avoided because of the large isolation between the working frequencies.

However, the current study proposes a three-coil based transmitter for the near field SWIPT applications. Where one coil is being utilised for power transfer and the two other coils are used for the information at two different frequencies. These two coils, working at two different frequencies, are called communication and test coil.

3.5.1 Design of the Transmitter front-end (Printed Coil Antenna)

Design and dimensions of the coils have been given in the figure below.

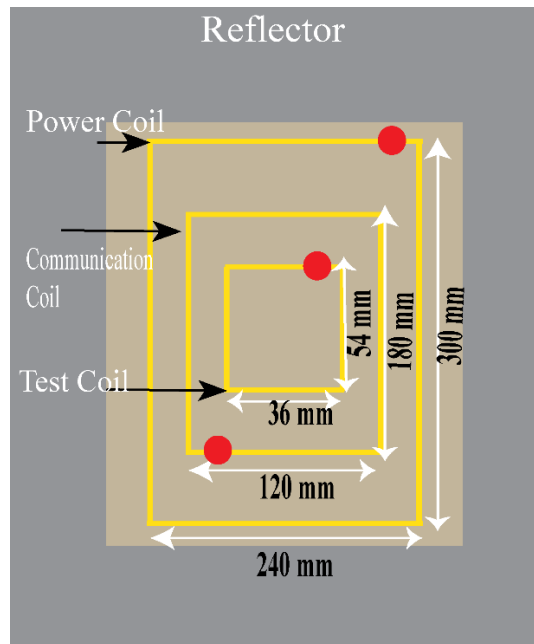


Figure 21 *SWIPT Transmitter*

These coils are designed on 3.5 mm thick FR-4 substrate. Copper is used for each coil having thickness of 70 μm and 7 mm trace width. Trace width and the thickness of the coil play an important role to optimize the losses. As increasing the thickness and width of the coil would reduce the losses

of the coils but at the same time it can be costly as well. Therefore, a trade-off has to be made between the cost and quality of the coils.

Red dots shown in Fig 21 are the indication of the feeding ports. These feeding points are placed on opposite side of the adjacent coils to have EM isolation of the coil. Similarly, inter coil distance and dimensions are also optimized.

Each coil is a single turn coil. Initially, the multiturn coil topologies have also been considered. Although multiturn coil ensures a greater flux however, they also lead to a lossy coil because of the additional resonance introduced by the multiturn. Increased losses in the coil lead to the loss of the efficiency as discussed earlier. Additionally, the power transmitter is not isolated in this case, rather it is colocated with two subsystems therefore single turn coil has been preferred over the other options.

Three different coils are working at different frequencies. The outer most coil represents the power transmitting one, working at 27MHz: it has to send the power to wake-up the inductively coupled receiving coil. It has inductance of 896 nH with a lumped series resonant capacitor of 38.5 pF. The inner two coils represent two co-located and independent subsystems working at 4MHz and at 6MHz, respectively: the first one is the communication coil, responsible for the reception of telegrams from the woken coil on the other side of the link. It is providing 398 nH of inductance, and 3.5 nF is the lumped series resonant capacitor. The smallest coil is placed for test purposes and does not need for high efficiencies.

To isolate the system from the surrounding, Aluminum reflector has been placed at a distance of 50 mm from the transmitter. These reflectors also help to reinforce magnetic flux between the coils and have positive impact on the link efficiency. The choices of the coils at 27MHz and 4MHz have been done according to the European rail traffic management system

ERTMS [55]. The Choice of the test coil is more of an auxiliary nature. It has been made sure that over all nature of the proposed work is inclined towards the existing practical application-based scenarios.

3.5.2 Description of the Problem

In real application based scenarios of IPT, most of the time we encounter a non-stationary scenario where transmitter or receiver might change their location with respect to each other. This movement compromises the efficiency of the system. The problem at hand is also one such case where a SWIPT system has to be optimized for the misalignment between the transmitter and receiver to provide the stable power transfer at a distance of 200 mm as shown in Fig. 22.

Changing the alignment of Tx and Rx results in changing coupling between them, which can reduce the efficiency of the system.

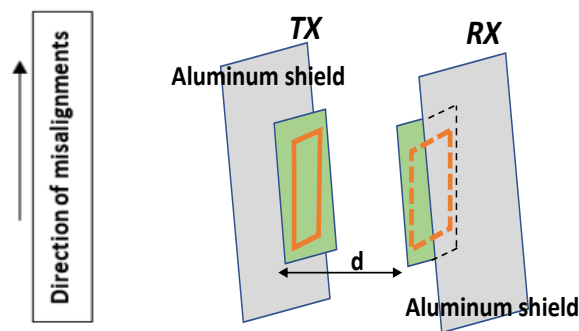


Figure 22 Misalignment of Transmitter at a constant d

Therefore, a wholistic approach has been adopted to optimize the entire WPT unit starting from choosing class E inverter, coil design and a generic receiver design.

Transmitter's dimensions are kept bigger than receiver which also helps to mitigate the effect of misalignment to some extent.

The other aspect of the proposed design is to take care of the efficient performance of the other sub-systems while primarily focussing on the WPT.

3.5.3 Design of the Amplifier

A similar Class E topology has been adopted as shown in Fig 23.

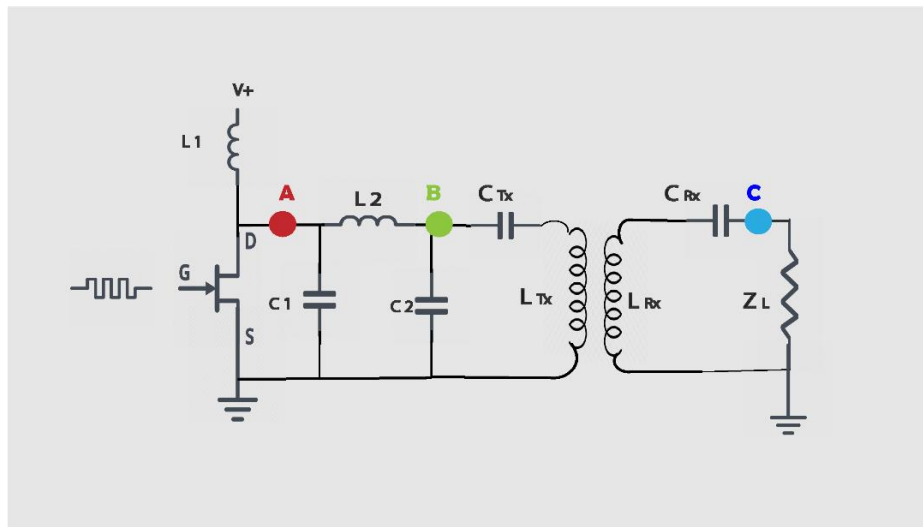


Figure 23 Entire IPT section with highlighted observation points

Where the matching network, used before the resonant Tx, plays an important role to compensate the effect of the changing distances between Tx and Rx and provide a matching condition for the load.

A 50%-duty-cycle-27MHz pulse is used to drive the gate terminal of the GaN-HEMT (GS66508b). The amplifier circuit is fed with a 9 V DC source and 50 Ω resistive load is connected at the receiver side.

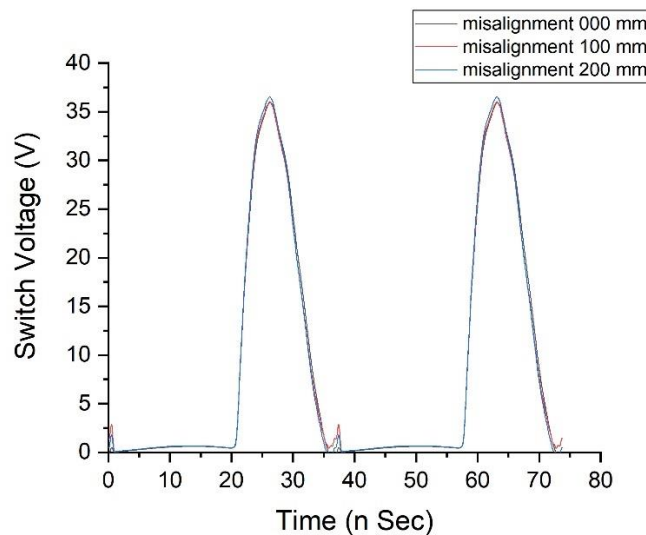
Inverter has been optimized using harmonic balance analysis. Compared to time domain transient analysis, HB technique can provide a deep inside into the steady-state behavior of the nonlinear circuit over the simulated harmonics. By knowing and controlling the frequency response of the circuit's linear part, HB technique allows to manipulate the steady-state

values of harmonic components of current and voltages: this is an added advantage for the designer to tailor different harmonics according to the requirement. After optimization, the pi matching network values are given as $C1=27.6\text{pf}$, $C2\ 20\text{pf}$, $L2= 8.7\ \text{nH}$.

3.5.4 Results and discussion for different misalignments at $d=200\text{mm}$

When the distance d as shown in the Fig. 22 is 200mm . WPT for different misalignments have been considered. The designed inverter has been able to provide a stable power, despite the misalignment between Tx and Rx.

Results for three cases with zero to $200\ \text{mm}$ misalignments will be presented here at the observation points A, B and C as highlighted in Fig.23.



18

Figure 24 Point A: Switch Voltage for different positions of the Tx

As shown in the Fig.24 ZVS condition is satisfied for all three positions of the Tx. It is interesting to see that not only that the ZVS condition is satisfied at different misalignments of Tx and Rx but also one can see that over all response shows minimum deviation for different misalignments.

Similarly, the voltage and current waveforms at point B i.e. at the transmitter are given as below.

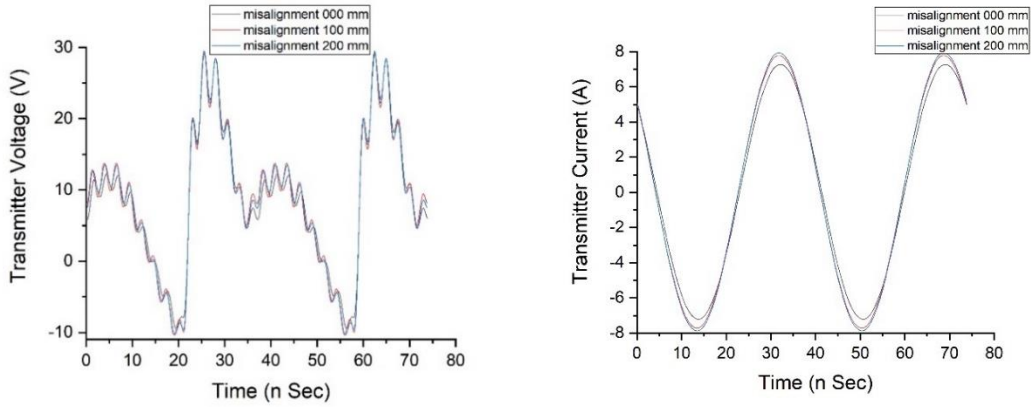


Figure 25. Voltage and Current Waveforms at point B

Voltage at the transmitter is composed of higher harmonics as can be seen from Fig.25. These higher harmonics are the result of nonlinear behaviour of the transistor working as a switch. These harmonics are filtered out by the resonance. However, Introduction of the resonance leads to high sinusoidal current amplitudes which create a strain on the transmitter. To distribute these high values current one can adopt a parallel combination of the resonant capacitor.

Point C as highlighted in Fig. 23 is at the receiver side. Corresponding Voltage and current values are shown as below.

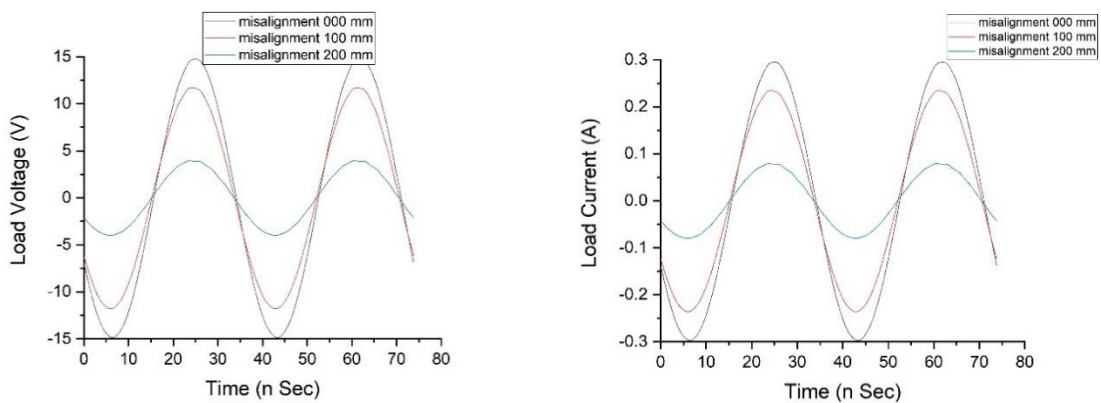


Figure 26 Load voltage and Current waveforms

The results shown in Fig. 26 represent the sinusoidal voltage and current waveforms. One can see that as the misalignment increases both current and voltage amplitude reduces which is the consequence of the reduced flux between the transmitter and receiver. Both Current and Voltage are in phase as well, which is the consequence of the choice of the real load.

3.5.5 Isolation of the Power Coil from the Co-located Subsystems

The presence of many subsystems gives rise to unwanted coupling among them. Without any precautions, most of the power at 27 MHz is coupled to other two coils present on the transmitter side; in particular with the communication one because of its proximity with the power coil. A strategic electromagnetic decoupling of the communication and the test coils from the power coil can be obtained through the placement of two trapping filters. These filters are parallel branches as shown in Fig. 27 (resonant at 27 MHz) connected in series with the communication and test coil in such a way that they present a very high impedance ($\approx 1.5 \text{ K}\Omega$) at 27MHz signal and a very small one ($\approx 200 \text{ m}\Omega$) at 6MHz and 4MHz, which are the operating frequencies for the two inner coils.

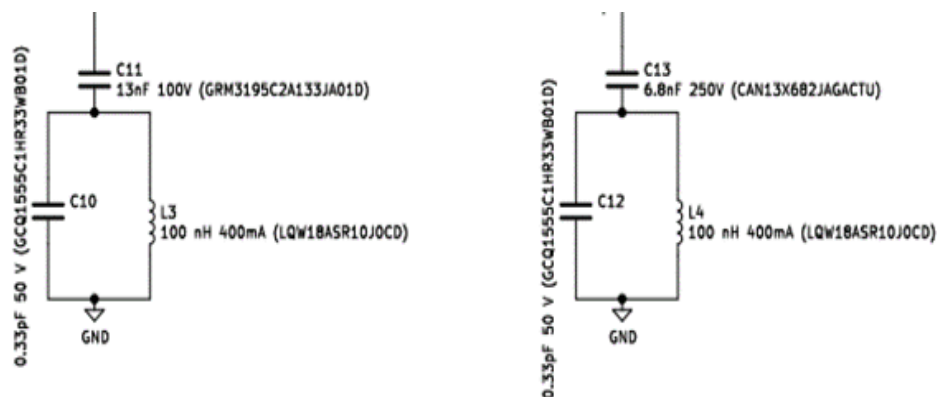


Figure 27 Trapping Filters for EM Isolation

Introduction of the trapping filters has improved the performance of the system. Table 2 shows the improvement achieved due to the trapping filter.

| | <i>Communication Coil</i> | <i>Test Coil</i> |
|--------------------------------|---------------------------|------------------|
| Before Trapping Filters | 19W | 0.07W |
| After Trapping Filter | 1W | 0.003 |

TABLE 2 *Coupled power for communication and test coils for different spacings*

3.5.6 Efficiency of the System

The efficiency of the proposed system is divided into two parts as shown in Fig. 28.

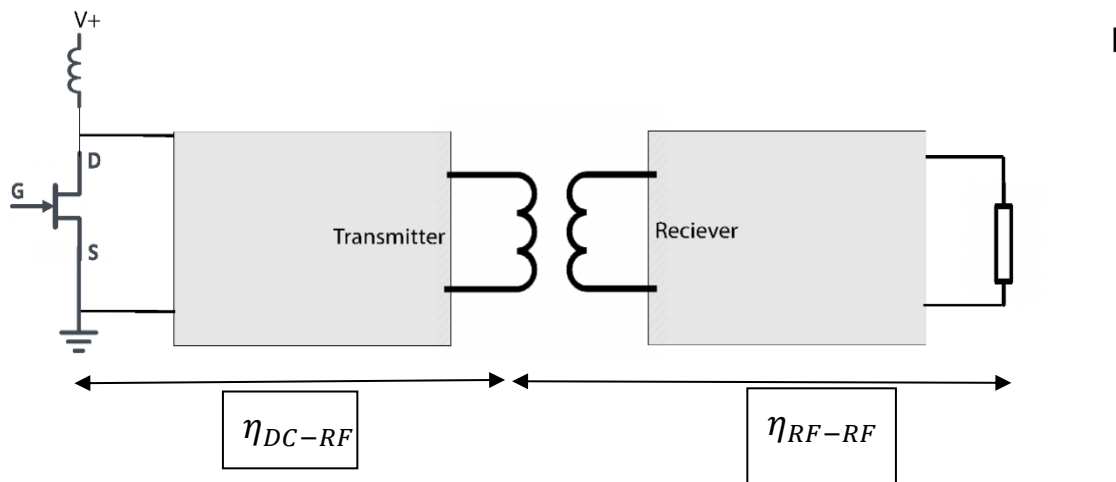


Figure 28 *Efficiency of the IPT system*

Efficiency of the system can be calculated from the power table 3 shown below. Power at different nodes as per Fig. 23 has been shown in the table.

| <i>Misalignment</i> | <i>DC Power(W)</i> | <i>Power at Tx (W)</i> | <i>Power at Rx (W)</i> |
|---------------------|--------------------|------------------------|------------------------|
| | <i>At node A</i> | <i>At node B</i> | <i>At node C</i> |
| 0 | 41 | 30 | 2.1 |
| 100 mm | 46.2 | 33.9 | 1.3 |
| 200 mm | 46.8 | 34 | 0.15 |

Table 3 Power Table for different misalignments at $d=200$ mm

Conversion Efficiency of the Amplifier:

Conversion efficiency of the PA is the ability of the amplifier to convert the input DC power to the output RF power. This efficiency is represented in Fig. 28 as η_{DC-RF} ,

$$\eta_c = \frac{P_B}{P_A} \quad (3.2)$$

η_c is around 73% .

Power Added efficiency:

PAE is another important aspect in the design of power amplifiers. It is defined as

$$\eta_{PAE} = \frac{P_B - P_{in}}{P_A} \quad (3.3)$$

Where P_{in} is the input RF power which is ~ 0.22 W in this case so η_{PAD} is around 72%

and η_{RF-RF} is dependent upon the links coupling condition and varies between 3% to 5%.

3.6 Driving Circuit

Driving of the GaN transistor is also important. Choice of GaN driver IC and the oscillator has been made depending upon their suitability to the current application under consideration. Driving Circuit is shown in Fig 29.

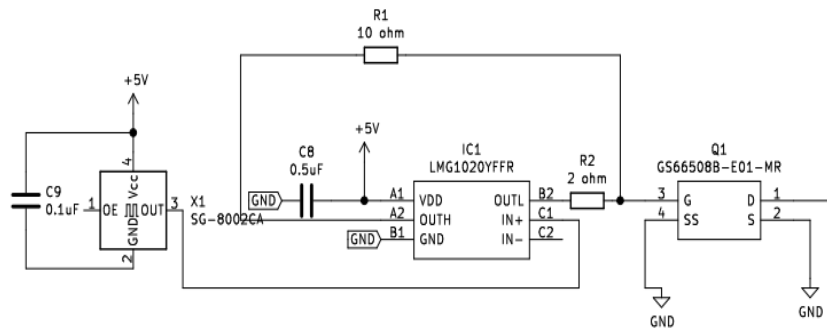


Figure 29. GaN driving schematic

3.7 Realization and Testing

The realization of the GaN driver together with the transmitter has been done and the performance evaluation of the proposed IPT is under observations as shown in the Fig.30.

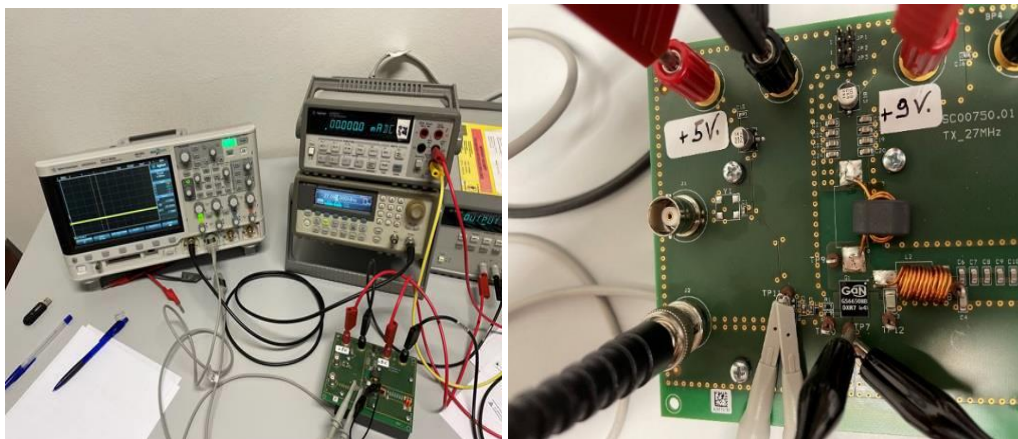


Figure 30 Inverter Performance Testing

Fig. 31 show the performance testing of the proposed SWIPT system. Oscilloscope screen shots are showing waveforms of the proposed transmitter.

Initially, the performance of the driving circuits has been verified to ensure the proper switching condition of GaN device. Then the performance of the switch has been analyzed under different load conditions.

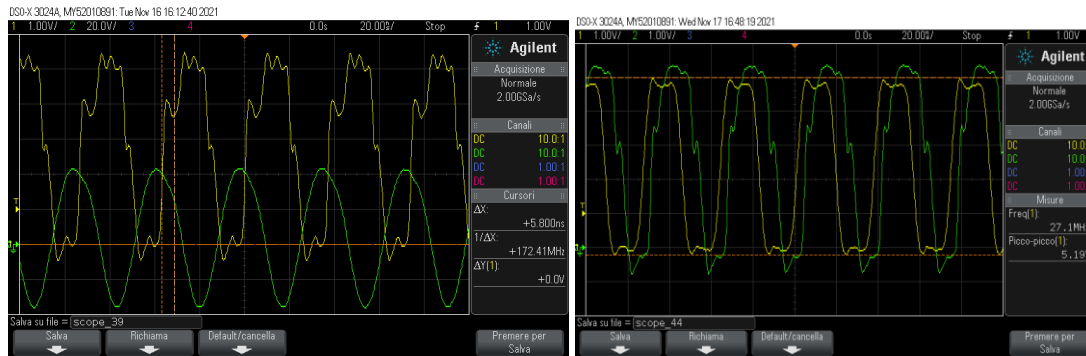


Figure 31 *Testing Waveforms for the inverter*

3.8 Conclusion and Future Prospect

This chapter aims at building the SWIPT systems for transport based applications. A systematic approach has been adopted for the SWIPT realization. Initially, to lay the foundation of IPT, a single coil Tx and Rx were considered. Then the design of three coil SWIPT and its different performance related aspects were discussed.

Three coils at the transmitter side have been designed and optimized to establish a link between Tx and Rx at distance 200 mm and for different misalignments.

Class E inverter has been adopted to power up the Tx-Rx link. Design of the inverter has been done so to take into account the misalignments between Tx and Rx and provide a stable power around 30W at the transmitter.

A trapping filter approach has been introduced to decouple the three coils present at the Tx side and to ensure the overall improvement of the SWIPT system.

This research activity can be further exploited in future to make it adoptable for the other applications which require the constant power at the receiver side for a moving transmitter. One way to could be to optimize the wireless link with the help of the additional coil to ensure the constant flux between the Tx and Rx.

CHAPTER 4

Intelligent Reflective Surfaces

4.0 Introduction

The concept and foundation of metamaterials were first time introduced by sir J.Pendry in 1999 [56] where he was able to explain that by just playing with the structural properties of the material, it is possible to manipulate electromagnetic waves. His idea revitalized the research in the area of electromagnetism and opened new horizons for the future research trends. The first experimental verification of the metamaterials came in 2001 when David Smith and the group were able to verify negative refraction of the EM waves by utilizing split ring resonators based 3D structure shown in Fig. 32. This was the earliest metamaterial.

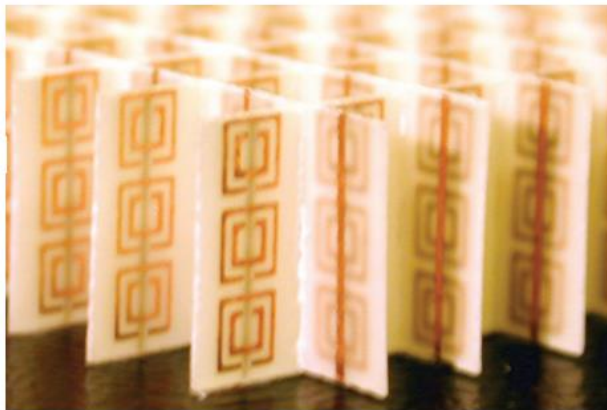


Figure 32 *First metamaterial structure by [57]*

Metamaterials have been around for more than two decades or so but recent years have seen a rising interest of the research community in this field because of its wide range of applicability. Metasurfaces are 2D conceptual realisation of metamaterials [58]. These surfaces are composed of meta-atoms or the unit cells which are of subwavelength size. These metasurfaces have the ability to manipulate the EM wave to achieve

fascinating results in terms of their functionality. Intelligent Reflective Surface (IRS) are also metasurfaces which can be used to manipulate EM waves to achieve non-specular reflection. An intelligent reflective surface is the one which can be reconfigured according to the needs. Reconfigurations of the such surfaces is achieved by controlling the response of each meta atom towards the impinging wave. Tuning the response of these metasurfaces can give rise to multifunctional metasurfaces which can be an absorber and/or a reflector [59,60] .

Reconfigurability of any metasurface can be divided into two categories [61].

1. Globally tuned MS
2. Locally tuned MS

4.1 Globally Tuned Metasurfaces

Globally tuned meta-surfaces (MSs) are responsive to external conditions and the entire metasurface changes its behaviour and achieves tunability. These external influencing factors can be of optical, electrical or mechanical nature. There are many research articles which have adopted this technique to achieve tunability of the MSs. [62] has realized a MS which consists of an array of unit cells connected with the pin diodes to achieve a two state tunability of the surface, which can perform as polarization converter working around 5GHz. [63] proposes metasurface which can perform as polarization converter and a simple reflector by introduction of pin diodes which can change the impedance and phase condition of the metasurface depending upon their on and off state. A transistor based tunability of the metasurface is reported in the [64] where metasurface works as an absorber and its absorption rates can be controlled through different biasing conditions of the active elements.

The response of the metasurface can also be changed by introducing materials as substrate which can change their properties under various applied conditions. [65] utilizes the semiconductor which changes its conductivity to change the response of metasurface at THz frequency ranges.

Similarly, there are other materials like Graphene liquid crystals and polymers used for the metasurfaces tunability for various frequency ranges [66,67,68].

4.2 Locally Tuned Metasurfaces

To achieve the beam scanning and effects like hologram, independent control of the each unit is important. Such metasurfaces are very complex structures which use impedance modulation over the entire metasurface to achieve exotic effects on the EM wave.

[69] presents a tunable wide band microwave metasurface which works as specular reflector with high efficiency between 2GHz to 7GHz frequency range. The author has used the diodes to control and optimize the response of the metasurface.

A similar concept has been used by [94] where the computer controlled ICs have been deployed between the meta-atoms which can provide a variable capacitance to make the MS act as an anomalous reflector. [70] presents a genetic algorithm-based metasurface which utilizes pin diode configuration to control the response of the individual meta-atom to achieve polarization conversion and beam steering functionalities. [71] has proposed a metasurface capable of generating holograms by carefully controlling the unit cells which are connected with the diodes. [72] utilizes an IC based approach for the metasurfaces which functions as an absorber for both TE and TM polarizations.

Many researchers are also focusing on the digital coded metasurfaces. The idea of the digital coding comes from the requirement of more than two states being available for the metasurface. Hence, instead of on-off states more states can be achieved using this methodology [73]. An FPGA based approach has been adopted by [74] to steer the scattered wave utilizing metasurface.

4.3 Applications of the Metasurfaces

Metasurfaces have provided an unparalleled control over the EM waves and over a large spectrum of the frequencies and both in linear and nonlinear functionality domains. Such a control is bound to have an impact over many next generation technologies in various fields.

Applications of the metasurfaces are many-fold, some major areas are highlighted under this section.

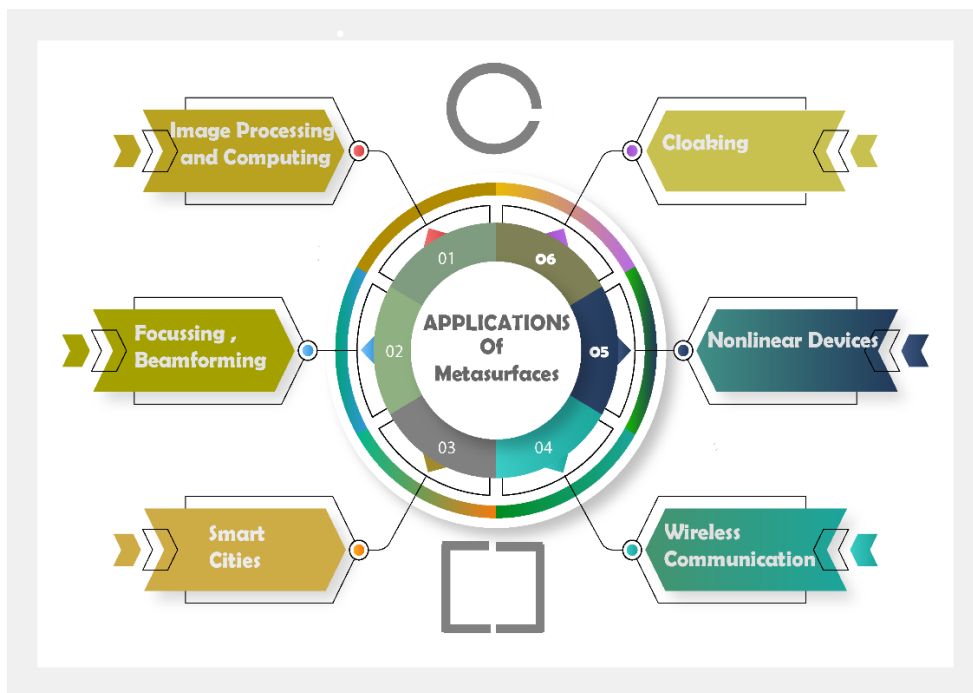


Figure 33 *Application Highlights* *²

² The graphic was taken from freepik.com and edited

The wireless communication field is going to benefit a lot from metasurfaces under the concept of smart radio environments. Such an environment is assisted by intelligent reconfigurable arrays of MS. Inclusion of the IRS in beyond 5G structures have been discussed and evaluated by many research groups [75,76] as a solution to enhance the coverage area. Inclusion of the RIS will make the control of the communication channel possible. [77] discusses the impact of IRS and channel models suitable to incorporate such metasurfaces.

Another important aspect of the IRS is beam steering and beam splitting [78]. Such properties of MSs are utilized to assist the localization as well as multi-user coverage [79].

The road to the smart cities of the future goes through the intelligent handling of the EM waves and, for that, metasurfaces are going to play an important part. Several application scenarios of the IRS assisted smart cities has been discussed in [80].

Metasurfaces are going to contribute in SWIPT systems as well. One such SWIPT system has been proposed for the unmanned aerial vehicles (UAVs) where IRS has been mounted on the UAVs and also around the surrounding infrastructure to enable efficient SWIPT [81]. We can expect that the future surveillance systems can benefit a lot from such technology. [82] also discusses the role of IRS to improve SWIPT systems.

Metasurfaces can also be designed to radiate the EM waves with good radiation efficiency. Highly directive leaky wave antennas are designed for controlling the surface wave by the modulated metasurface [83]. Such antennas find their applications in radars [84]. Use of the metasurface in guiding structures can help them reduce their sizes [85].

Metasurfaces have found their application in the field of image processing as well. The hologram is a technique to reproduce the image of an object by amplitude and phase information of EM wave [86].

Information of the polarisation is an important factor in many communication systems. Therefore, manipulation of the polarisation is an important ability to achieve. This capability has been reported quite extensively by the use of polarization sensitive metasurfaces [87,88,89].

Making an object optically invisible has long been a fictional idea. However, in 2006 J Pendry proposed the idea of cloaking by controlling the EM waves [90]. Since then a lot of research has been done in that direction to achieve cloaking from microwave to optical regime [91,92].

Metasurfaces can also be utilized for non-linear functionality for example generation of higher harmonics [93].

The metasurfaces with their unique properties have many other applications as well. In future one can expect that these applications are going to increase because of the special nature of the metasurfaces.

4.4 Intelligent Anomalous Reflector

A reflector which can reflect the incident EM wave to a non-specular direction is called as anomalous reflector. Such a reflector is made by the deployment of the metasurfaces. As established in the earlier section, to achieve more functionalities from the metasurfaces the trend is to make them reconfigurable. Such a metasurface is known as the intelligent metasurface.

Here we are going to discuss a case study of an intelligent anomalous reflector [94] to lay the foundation and understanding of our work in the coming chapter. It is worth mentioning that results of the [94] that are being shown in Fig. 34, Fig. 35, Fig. 38 are reproduced in order to have the

understanding of the proposed technique and to lay a foundation for the proposed work in Chapter 5.

A simple square patch topology has been adopted to make a reflector which is working in the microwave region. Dimensions of the unit cell are being shown in Fig. 34.

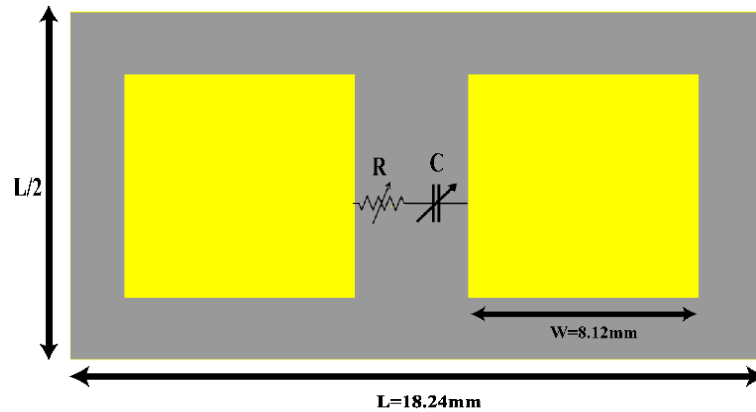


Figure 34 Unit cell design

Copper is used for both patches and ground and RT5880 is used as the substrate with height of 1.016 mm for the unit cell. It is important to have a local control of the unit cell which is also known as the meta-atom. To have a fully local control of the metasurface, it is important to have the control over the impedance of the meta-atoms. Therefore, variable capacitances and variable resistances are connected to tune the performance of the meta surface.

The proposed meta-surface works as a tunable perfect absorber (TPA) as well as tunable anomalous reflector.

4.5 Working Principle

Performance of the metasurface depends upon resonance due to the impedance control of the unit cell which in this case is the control of the capacitance and resistor values connected in series with the patches. The

variation of the capacitance can provide the control over the resonant frequency and changing the values of the variable resistor provide us the control over the magnitude of reflection and absorption as shown in Fig.35.

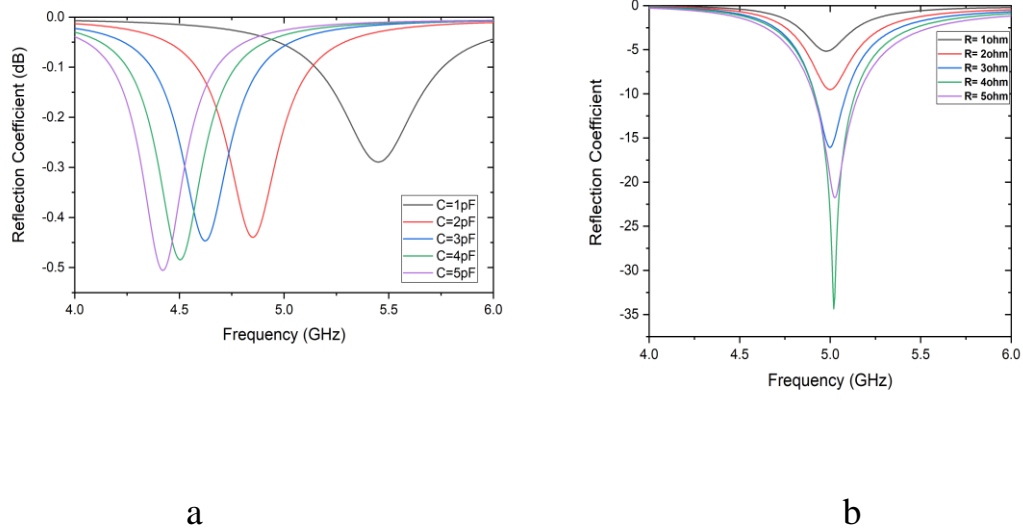


Figure 35 Reproduced results for the Variation of C (a) and R (b) values and their impact on Reflection coefficient.

The realization of the absorber is straightforward, but for the realization of the anomalous reflector there are other aspects to be taken care off. First of all, we need to keep the size of the unit cell much less than the wavelength and there should be phase span of the wave reflected by the surface as wide as possible. These two parameters (i.e., size and phase) play a fundamental role in the realization of the anomalous reflector.

Fig. 36 shows the reflection phase and the amplitude of the wave reflected by the uniform metasurface as function of the tunable capacitance. Variation of the capacitance values from 1 pF to 5 pF provides wide phase change and the reflection coefficient remains very high throughout. Here, operating frequency of the surface is considered to be 5 GHz.

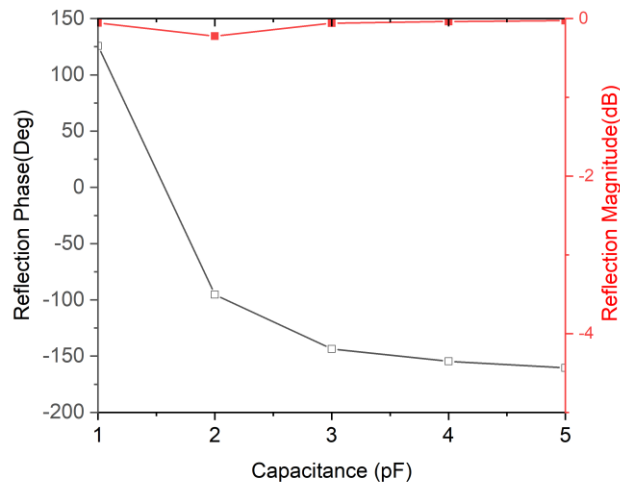


Figure 36 Phase and magnitude of reflection coefficient [94]

The efficiency of the reflector can be further increased by adopting the super cell approach. Super cell is composed of more than one sub wavelength unit cells. Increasing the number of unit cells reduces the parasitic reflections and increases the efficiency of the anomalous reflector.

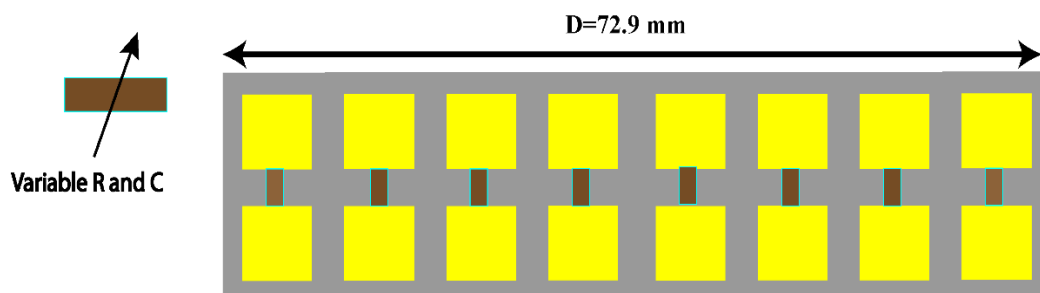


Figure 37 Super Cell dimensions [94]

Super cell shown in the Fig. 37 consists of 8 unit cells. Each unit cell has same dimensions as shown in the Fig.34. While the capacitances connected in series with the patches are varied in linear fashion.

When a plane wave is excited at normal incidence at the supercell, number of diffraction waves of different order are scattered from the surface. Number of diffraction orders depends upon the size of the super cell.

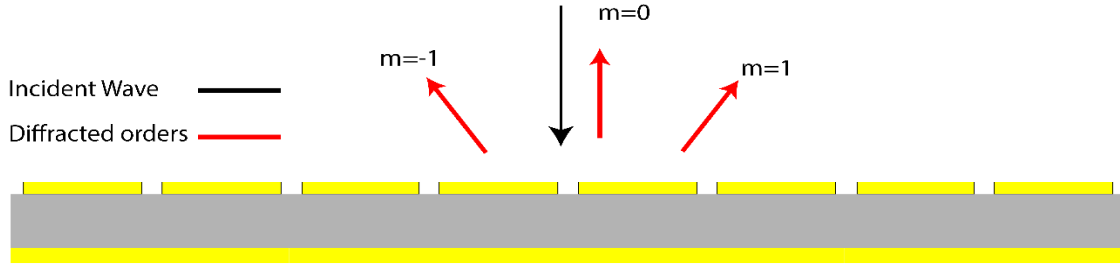


Figure 38 Three diffraction orders for 8 element-based super cell

Angle of diffraction orders for the normal incidence can be calculated from the following equation.

$$\theta = \sin^{-1} (m\lambda_0)/D \dots\dots\dots (4.1)$$

Above equation indicates that to achieve wider reflection angle range we need to increase the size D of the supercell. Reflection angle of diffraction orders $m=\pm 1$ is $\pm 55.3^\circ$ in the case of the supercell of Fig. 37.

As incident power is coupled to more than one diffracting order, hence, to improve the efficiency of the anomalous reflector we need to suppress the power coupled to the unwanted directions. Therefore, we need to optimize the impedance of the supercell by optimizing the variable capacitance values. A linear variation of the capacitance values has been selected in the current case of supercell [94].

Floquet port analysis of the supercell has been done by adopting the electromagnetic software HFSS. Floquet port analysis is used for the periodic planar structure where a high number of modes can be excited (one Floquet port per mode is selected.). TE polarized wave has been selected as the normal incident wave.

Values of the capacitors are optimized in [94] such that the reflection coefficient associated with $m=1$ is maximized.

S-parameter results of the optimized structure are shown below.

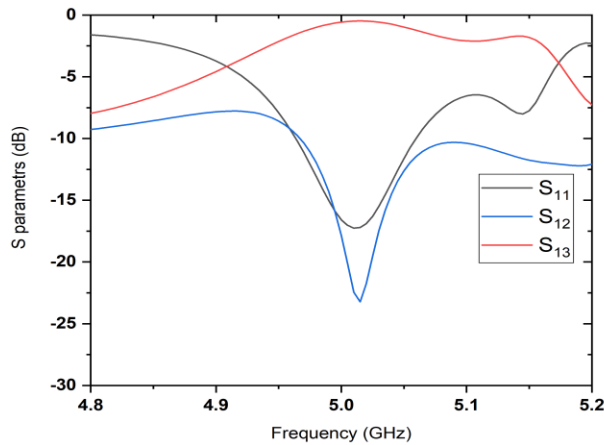


Figure 39 *Optimized reflection magnitudes of 3 diffraction orders*

Fig. 39 shows the reflection of the diffraction orders where S_{11} represents the standard reflection at $m=0$, and S_{12} and S_{13} are representing $m=-1$ and $m=+1$, respectively. Fig. 38 shows that at 5 GHz maximum power is being coupled to the diffracted order with $m=1$ by suppressing other unwanted reflection amplitudes. Efficiency of the system is given by the following equation.

$$\eta = |S_{13}|^2 / \sum_{i=1}^3 |S_{i1}|^2 \dots\dots\dots (4.2)$$

Efficiency of the anomalous reflector under consideration is 95% [94].

4.6 Conclusion

In this chapter a brief introduction to the metasurface has been given. The importance of the metasurfaces under the light of current research advancement and trends has been established. Then an example of the an anomalous reflector has been verified to lay the foundation and working principle for the reconfigurable anomalous reflector to be designed in the next chapter.

CHAPTER 5

Design of Metasurface Based Polarization Converter and IRS

This chapter is based on the following article

[106] S. Agarwal, G. Murtaza, A. Costanzo and D. Masotti, "A Super Wideband Angularly Stable Metasurface for Cross Polarization Conversion Applications," 2021 International Microwave and RF Conference (IMaRC), 2021.

5.0 Introduction

Polarization of the EM waves provides additional information on the channel for many communication scenarios. Therefore, it is important to have the control over polarization of the EM waves. As discussed in the previous chapter, metamaterials provide us also the flexibility of the manipulation of the polarization of the EM wave. Metamaterial-based polarization converters have been discussed extensively in the literature, in broader frequency spectrum, ranging from microwave to the optical frequencies.

5.1 Working Principle

From the Faraday's law, we know that when the time-varying magnetic field passes through a loop of the conductor wire, it produces the current in the loop itself. Pendry in 1999 showed that when we introduced a cut to break the symmetry of the loop that structure behaves as a resonant structure.

When we excite an EM wave on such a structure at its natural frequency such a resonance produces negative magnetic response, which means that

although the proposed resonant ring is not made of materials with negative permeability but the effective permeability of the structure was able to achieve negative values [95]. Such a response is not found in the natural materials. In addition to that, this resonance is the function of the geometrical parameters of the structure which we can be controlled to our advantage. Such a structure is known as the split ring resonator which is the basic building block of many metastructures. Fig.40 shows a circular split ring resonator.

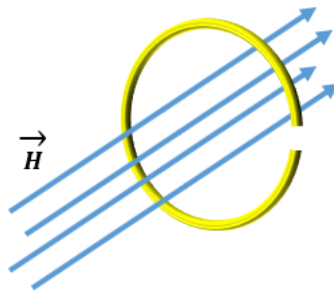


Figure 40 *Split Ring Resonator*

Until 2004 it was believed that EM wave can only produce resonance when \mathbf{H} is perpendicular to the SRR. However [95] showed that it is also possible when incident electric field is aligned along the gap bearing side of the SRR. Fig 41 shows that the electric field along the broken mirror symmetry of the SRR produces the current circulation even if \mathbf{H} field is not perpendicular to the SRR. Therefore, we can use this principle to our advantage in the design of metasurfaces.

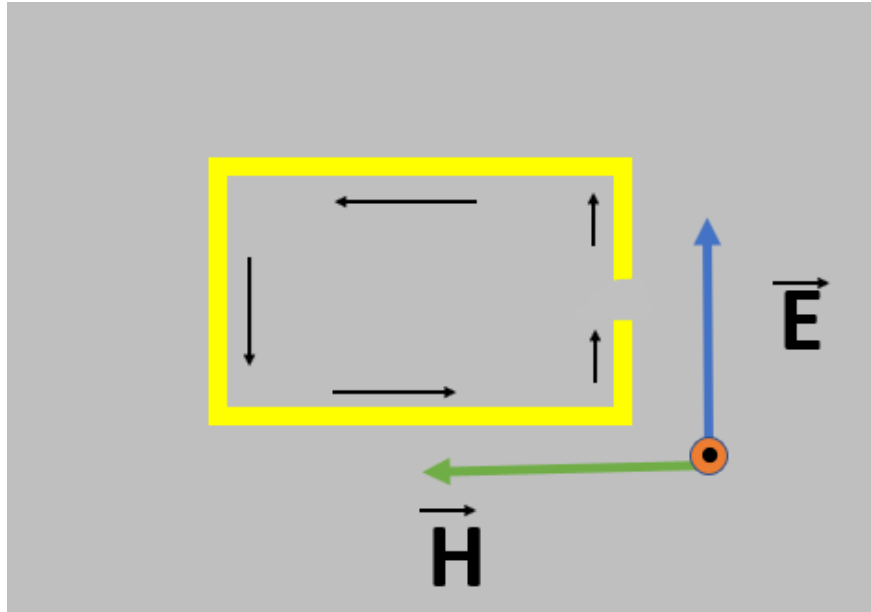


Figure 41 Representation of the Electric Field along gap bearing side of SRR

5.2 Proposed Design of the Polarization Converter

A low-loss dielectric substrate Rogers/RT 5880 with dielectric constant $\epsilon_r=2.2$, height $h=2.4\text{mm}$, and $\tan\delta=0.0009$ is used to design the proposed metasurface: aim of this activity is to reach a super-wideband polarization converter deploying a metasurface. Impact of the SRR on the co-polarized and cross-polarized incident field has been first verified as shown in the Fig.42.

Co-polarised reflection coefficient (R_{xx}), is the ratio of the amplitude of electric field of the X-polarized reflected wave to the X-polarized incident wave and Cross-polarized reflection coefficient (R_{yx}) represents the ratio of amplitude of E (electric field) of Y-polarized reflected wave to the X-polarized incident wave.

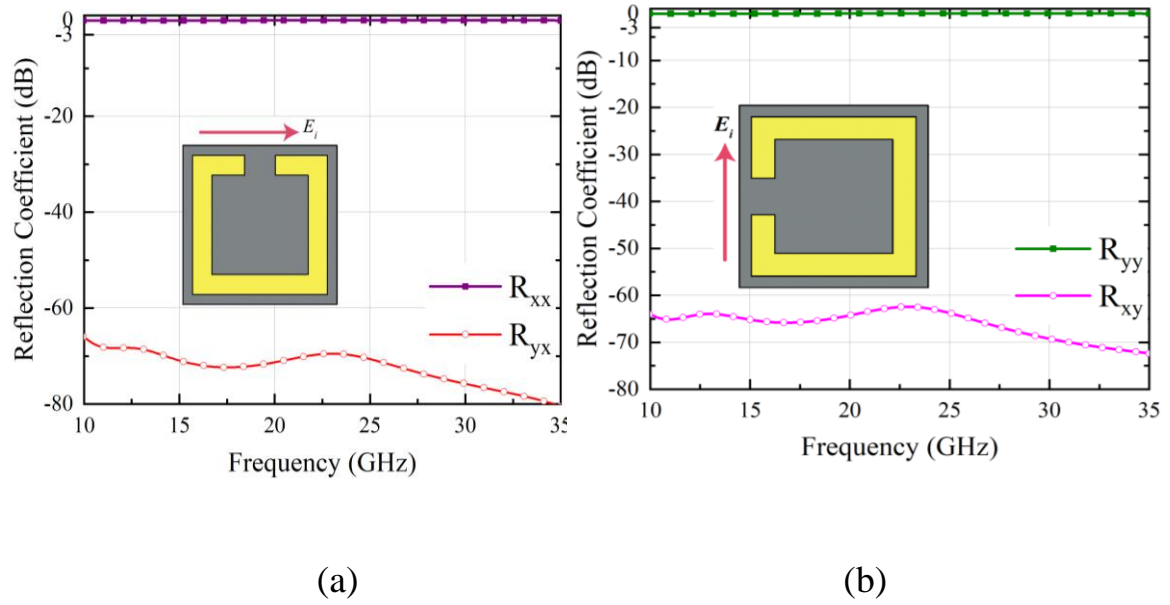


Figure 42 Co-polarized and cross-polarized reflection coefficient for single split cell (a) X-polarized wave (b) Y-polarized wave [106]

As it can be seen in Fig. 42, that for X polarized incident wave along the gap bearing side cross polarization is suppressed and vice-versa.

Using this known technique, two gaps are introduced in the adjacent sides of the proposed design of square SRR, one for each linearly polarized impinging field, thus achieving a dual-polarization converter. An additional new idea, a circular ring resonator has been placed inside the square one. This additional smaller resonator allows to have resonance also at higher frequency which leads to widen the bandwidth of the proposed polarization converter. Fig . 43 shows the dimension and other geometrical parameters of the proposed design.

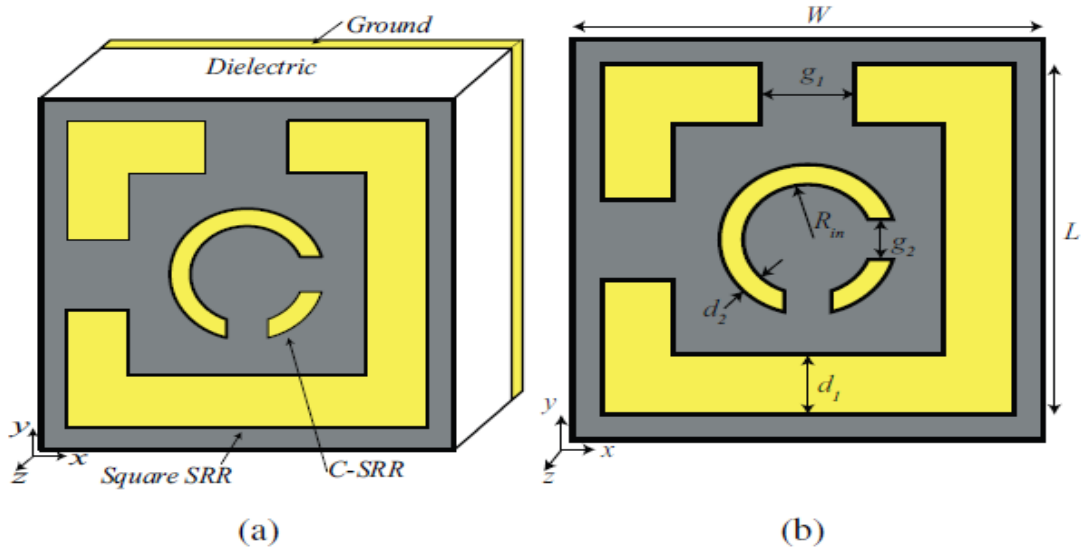


Figure 43 proposed metasurface [106] (a) Perspective View (b) Front view.

The other side of the substrate is backed by full ground plane. A standard copper of 35 microns is used to design the SRRs and the ground plane.

The structure has been optimized and simulated by adopting the electromagnetic software simulator CST Microwave Studio, using the Floquet port as excitation along the +Z axis and applying the proper periodic boundary conditions along X and Y axis. In CST unit Cell boundary conditions are established along X and Y axis. Unit Cell boundary condition are used for periodic structures, to mimic infinite periodic structures.

Optimized values of the metasurface are shown in the following table 4.

Table 4

OPTIMIZED DIMENSIONS OF THE PROPOSED METASURFACE

| <i>Parameters</i> | <i>Value (mm)</i> | <i>Parameters</i> | <i>Value (mm)</i> |
|-------------------|-------------------|-------------------|-------------------|
| w | 4 | d_2 | 0.2 |
| L | 3.5 | g_1 | 0.8 |
| d_1 | 0.6 | g_2 | 0.4 |
| R_{in} | 0.55 | - | - |

5.3 Results and Discussion

When an X-polarized wave is made incident on the metasurface, co-polarized and cross-polarized components are produced.

Mathematically, co-polarized and cross-polarized components are defined as

$$R_{xx} = \frac{E_{rx}}{E_{ix}} \quad (5.1)$$

and

$$R_{yx} = \frac{E_{ry}}{E_{ix}} \quad (5.2)$$

where the subscripts i and r stay for incident and reflected, respectively.

Similar equations are defined for the Y-polarized incident wave. Two corresponding ratios are defined as R_{yy} (co-polarized) and R_{xy} (cross-polarized).

The efficiency of the polarization conversion is measured with the Polarization Conversion Ratio (PCR) which is defined as

$$PCR = \frac{|R_{yx}|^2}{|R_{xx}|^2 + |R_{yx}|^2} \quad (5.3)$$

The simulation results for the proposed metasurface for X- and Y-polarized waves are shown in Fig. 44 (a) and (b), respectively.

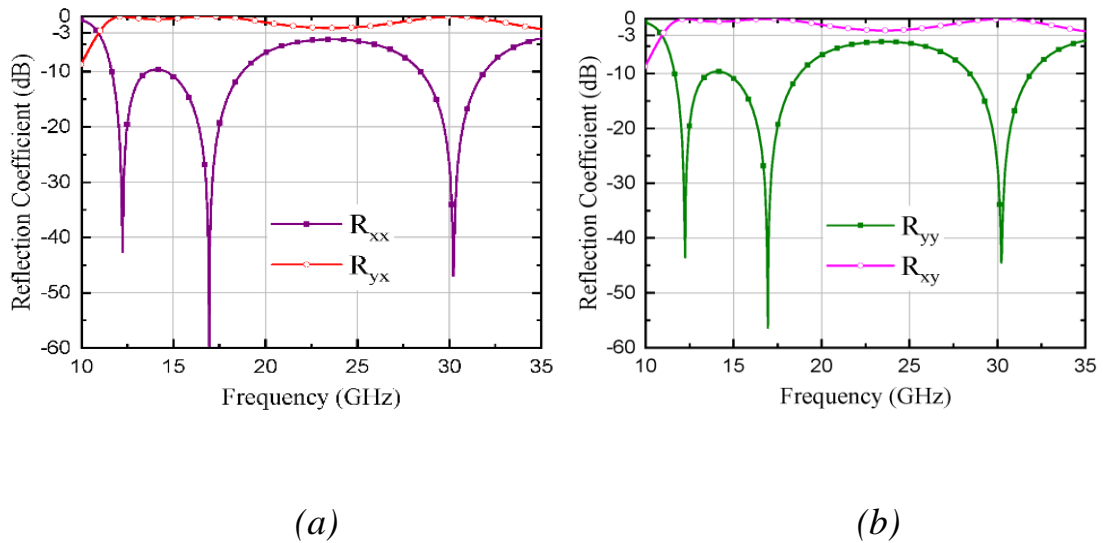


Figure 44 Reflection coefficient of X (a) and Y (b) polarized incident waves

It can be observed from Fig. 44 (a) that the proposed metasurface is operating from 11GHz - 35GHz with three resonances at 12.24, 16.95, and 30.22GHz respectively. At these frequencies, the metasurface is behaving as an almost perfect polarization converter. Similarly, for a Y-polarized wave, Fig. 44(b) displays the co-polarized and cross-polarized components. The proposed metasurface works perfectly for the entire range of frequencies of vertically polarized wave, as illustrated in the figure.

PCR vs frequency response is displayed in Fig. 45 to validate the suggested metasurface's polarization conversion efficiency.

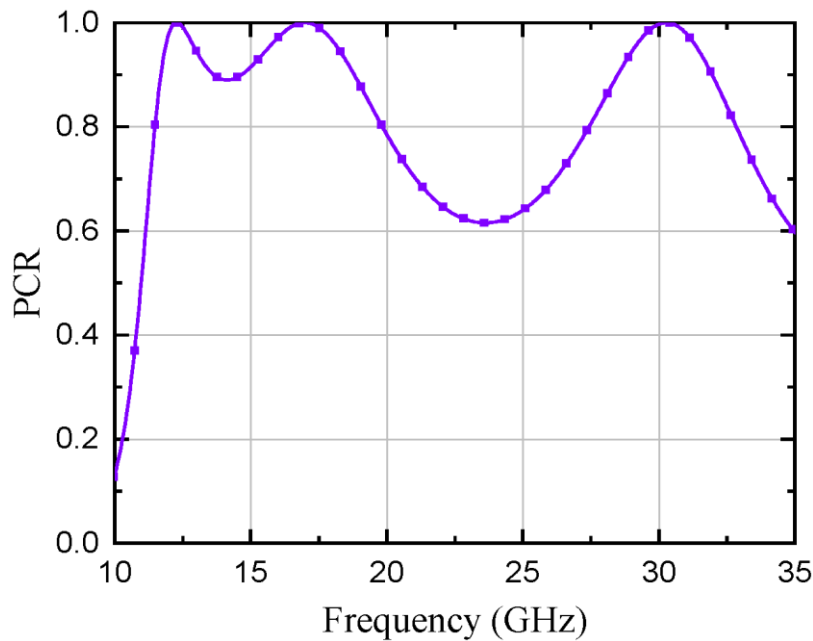


Figure 45 *PCR vs frequency*

The figure shows that PCR is consistently above the threshold value of 0.6 throughout the operational range. It also has three peaks at three resonances (12.24GHz, 16.95GHz, and 30.22GHz), and it functions as a nearly perfect polarization converter at these frequencies. These results demonstrate the unprecedented super-wideband behaviour of this metasurface.

5.4 Angular Stability of the Metasurface

Normal incident waves in a practical environment are very rare. The metasurfaces must also respond to oblique incident waves in order to meet this requirement.

The proposed metasurface is investigated for horizontally and vertically polarized waves with an oblique incidence of up to 40 degrees.

Fig. 46 (a) and (b) illustrate the simulation findings for co- and cross-polarized components for X-polarized waves, respectively.

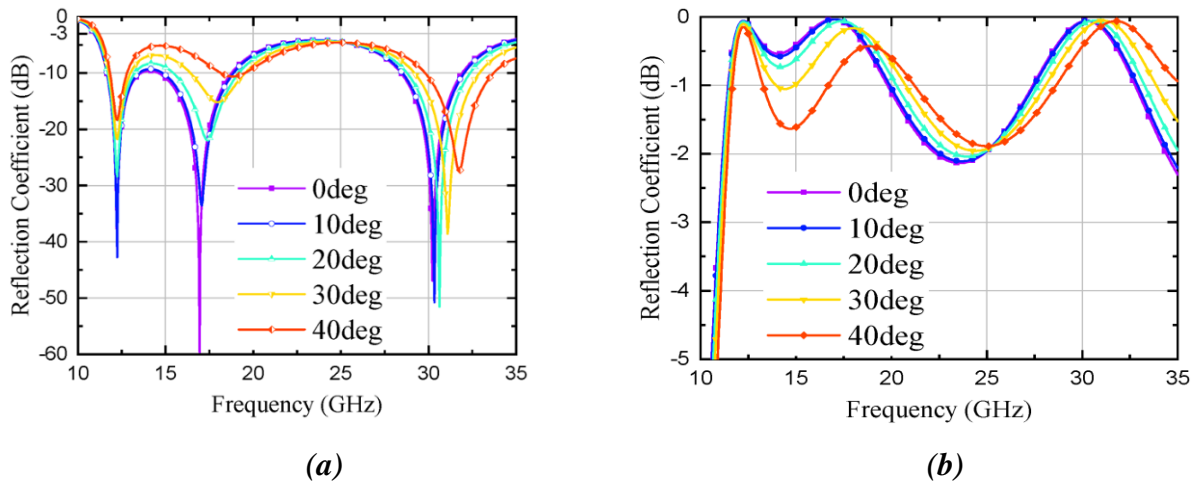


Figure 46 Angular stability response for oblique incidence (a) R_{xx} (b) R_{yx}

Similarly, for vertically polarized wave, Fig. 47 shows good angular stability for a large range of incident angles.

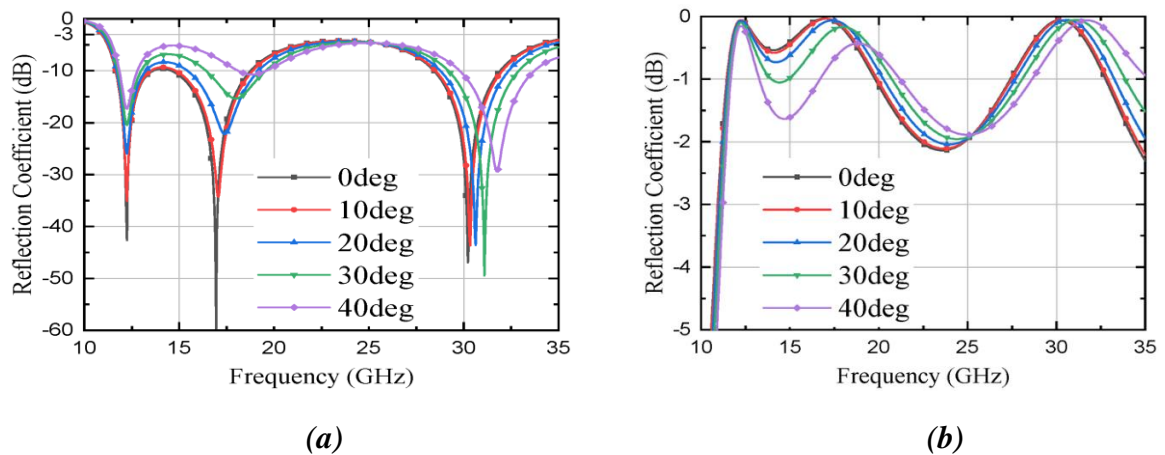


Figure 47 Angular stability response for oblique incidence (a) R_{yy} (b) R_{xy}

5.5 Reflection Angle Measurement

Knowledge of the reflected angle is some time important for some application scenarios. However, there is a lack of information in the literature about metasurface excitation and reflection angle measurement.

In view of this, this section examines a method for determining the reflection angle. The research was carried out on three different metasurface configurations: 3x3, 6x6, and 9x9. For varied values of incidence angle, and with a plane wave excitation source employed to excite the metasurface.

Fig.48 (a) and (b) depict a schematic of the metasurface and the accompanying simulation setup, respectively.

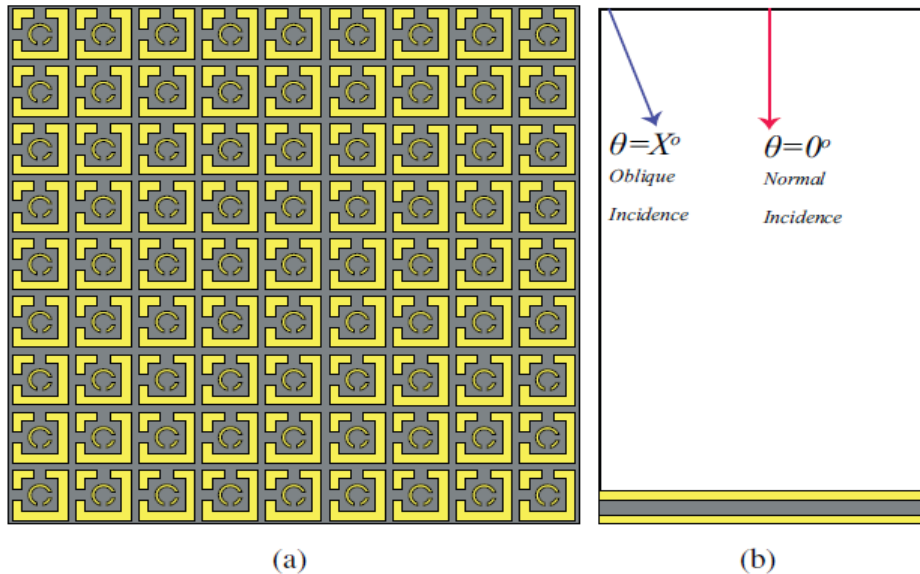


Figure 48 (a) 9x9 array of proposed metasurface, (b) simulation setup (Proposed [106])

The simulation is performed for various values of incidence angle; the results are discussed only for normal incidence ($\theta_i=0^\circ$) and two oblique incidences $\theta_i=15^\circ$ and $\theta_i=60^\circ$ to see the performance of metasurface for reflection angle measurement.

Results for 3x3, 6x6 and 9x9 array for different incident angles are shown in Fig. 47,48, and 49, respectively. For normal incidence in all the cases, the direction of the reflected beam is at $\theta_r=0^\circ$ while for oblique incidence case the beam is observed at $\theta_r=15^\circ$, hence it obeys to the reflection law. Furthermore, for incidence angle $\theta_i=60^\circ$ the reflected beam angle changes with frequency and also is not equal to the incidence angle. From these figures, it can be confirmed that the proposed metasurface is stable for an oblique incidence around $\theta_i=40^\circ$, as previously established. To evaluate the polarization conversion of the metasurface by means of this rigorous full-wave approach (just to doublecheck the unit-cell approach previously adopted), the size of the metasurface would need to be of several wavelengths, hence a matrix of at least 50x50 cells would have been needed, which was not possible due to lack of available facilities. Furthermore, for the cases $\theta_i=0^\circ, 15^\circ$ it can be concluded that as the size of the metasurface increases, the reflected beam starts shrinking which indicates that the gain increases with the increase in array size. This is due to the fact that as area increases, more power falls (less spillover) on the metasurface and strong reflection are observed, accordingly.

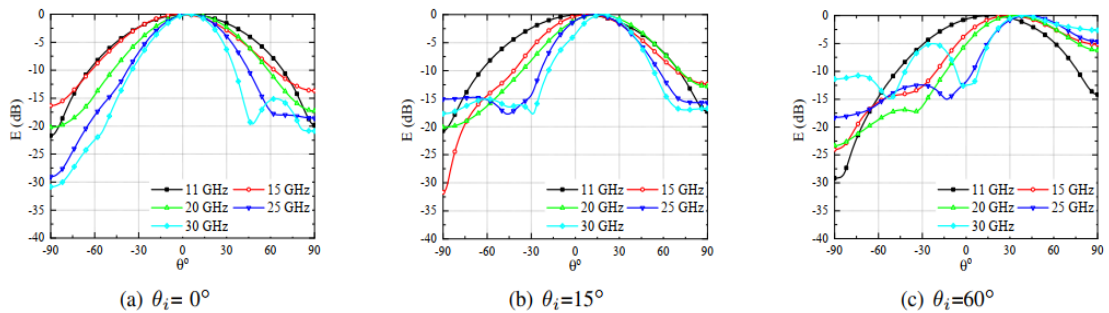


Figure 49 Reflection angle measurement for 3x3 array (Proposed [106])

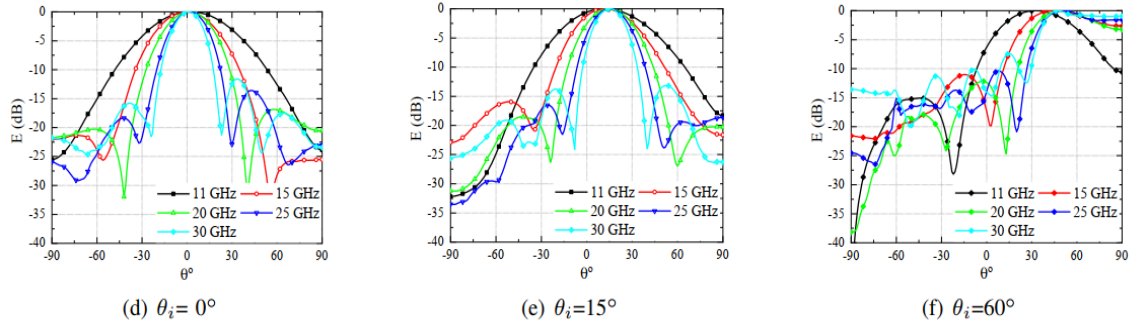


Figure 50 Reflection angle measurement for 6x6 array (Proposed [106])

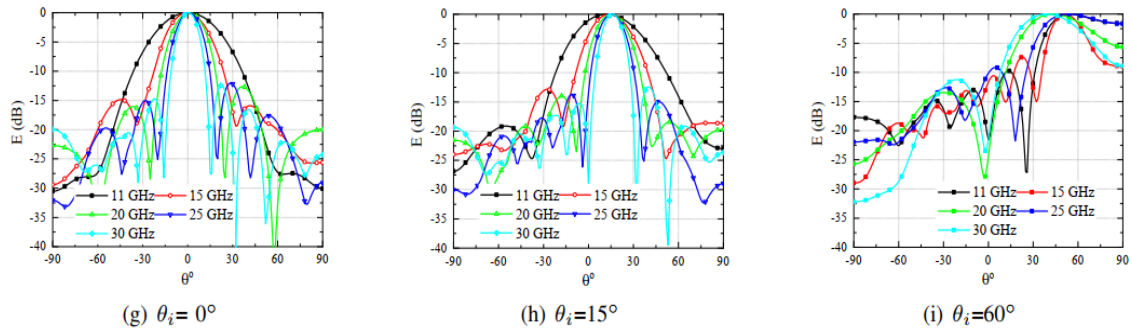


Figure 51 Reflection angle measurement for 9x9 array (Proposed [106]).

Size of the meta surface and bandwidth has been compared with already published results [96-104]. It is evident from comparison table that the proposed design has higher bandwidth and compact size.

Table 5

COMPARISON OF THE PROPOSED METASURFACE WITH PREVIOUS WORKS

| Reference Articles | Bandwidth (GHz) | Size (%) compared to the proposed work |
|--------------------|--------------------------|--|
| [96] | 5 - 9.7 & 11.2 - 15 | 67.3 |
| [97] | 7 - 9.18 & 11.66 - 20.40 | 84 |
| [98] | 16 - 32 | 36 |
| [99] | 6.7 - 20.7 | 84 |
| [100] | 6.2 - 24.3 | 55.5 |
| [101] | 5 - 15 | 67.3 |
| [102] | 4.2 - 13.9 | 84 |
| [103] | 7.4 - 10.5 & 12.7 - 20 | 67 |
| [104] | 5.7 - 11.4 | 84 |
| Proposed [106] | 10.92 - 35 | - |

5.6.0 Globally Tuned IRS

Intelligent reflective surfaces have attracted a great deal of attention of the scientific community to achieve full control over the EM wave manipulation. Current advancement of the communication systems especially under beyond 5G scenarios and SWIPT systems demand an intelligent EM environment. Provision of the IRS to enable the concept of smart cities under the umbrella of IoT is necessary.

One of the important aspects of the IRSs is their ability to be reconfigured to achieve multifunctional status. There are two types of reconfigurable IRS which include the globally tuned and locally tuned surfaces. Local tuning of the IRS is a complex way to achieve reconfigurability. Therefore, for the sake of current study the globally tuned IRS has been under considerations. There are many ways in which the notion of global reconfigurability is catered including the mechanical and thermal tuning and applied external voltage. One of the most frequently used method is the use of pin diodes to have an ON-OFF or binary control over the impedance variation of the metasurface.

Ideally one would like to have a continuous control over the impedance change of the metasurface to manipulate the incident EM wave. However, pin-diode approach only presents some discrete set of variations which makes the scope of such surfaces very limited.

5.6.1 Introduction to Proposed IRS

For the current study although a globally tuned metasurface is under consideration but to achieve the continuous control over the impedance of the IRS a different approach has been adopted.

A simplistic square patched super cell approach has been adopted [94] as discussed in the previous chapter. However, instead of commutator-controlled IC approach to change the impedance between the patches, an interdigitated capacitor (IDC) approach has been adopted. To have the continuous control of the impedance a thin layer of the HfZrO has been proposed which can change its properties with the magnitude of applied voltage.

5.6.2 Tunability and Zirconium-doped Hafnium oxide (HfZrO)

With the advancement of the technology, a whole new class of materials have emerged over the last decade which have very useful intrinsic properties. HfZrO is one such material which is known for its properties suited for the microwave application and widely studied and exploited within the framework of the H2020-NANO-EH European project, whose consortium includes the Department of Electrical, Electronic and Information Engineering.

HfZrO is a ferroelectric material that can change its relative permittivity under the applied voltage in a continuous fashion. [105] has reported the electrical property of HfZrO in the microwave range. It is highly dispersive in nature as it changes the relative permittivity value significantly with the frequency.

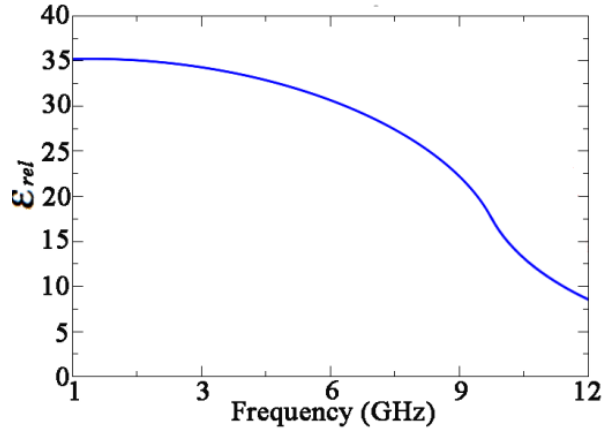


Figure 52 Variation of the relative permittivity of the HfZrO vs frequency [105]

There are many advantages that HfZrO brings on the table. For example, it is CMOS compatible which makes it suitable candidate for the large-scale fabrication. Its thickness is of nano scale order which can be used in compact and thin substrate application; moreover, it has ferroelectric effects for low voltages, and it shows tunability at low applied DC voltages around $\pm 5V$. Measured data of the ferroelectric behaviour of the HfZrO have been provided by the partners of the NANO-EH consortium and are reported in the following table:

Table 6 Measured data for Change of permittivity of HfZrO with different biasing conditions

| Applied Voltage across HfZrO | Relative Permittivity of HfZrO | Tan(D) |
|------------------------------|--------------------------------|---------------|
| <i>Un-biased</i> | <i>14.47</i> | <i>0.0226</i> |
| <i>1V</i> | <i>19.87</i> | <i>0.0230</i> |
| <i>2V</i> | <i>26.74</i> | <i>0.0236</i> |
| <i>3V</i> | <i>35.07</i> | <i>0.0260</i> |
| <i>4V</i> | <i>44.87</i> | <i>0.0275</i> |
| <i>5V</i> | <i>54.95</i> | <i>0.0285</i> |

5.6.3 Proposed Design of the IRS

To exploit the tunability properties, a thin layer of HfZrO over the silicon substrate has been used. Fig. 53 shows the proposed design of the unit cell.

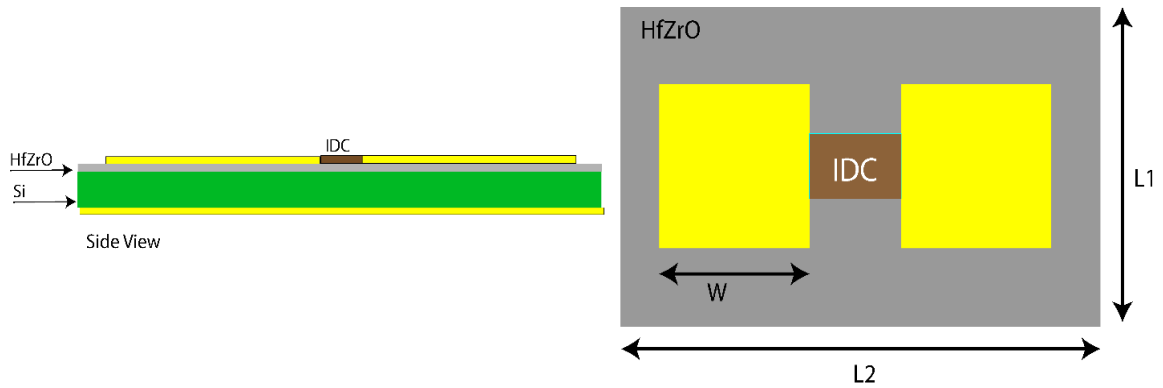


Figure 53 Side view and front view scheme of proposed Unit Cell

Very thin layer (10 nm to 20 nm) is applied above the Silicon substrate of $60 \mu\text{m}$, because thicker layers of HfZrO have demonstrated to lose the ferroelectric property. These Stack up values have been obtained through constant optimization of different substrate heights to ensure better performance. L_2 is 14.5 mm and L_1 is kept half of L_2 . Square patches are placed on the thin layer of the HfZrO and connected with the IDC. As per the methodology established in chapter 4, the phase requirement of the unit cell has been found and variations of the resonance phenomenon with changing capacitances has been done as shown in the Fig. 54. Initially, the lumped values of the capacitances have been selected. Which will be replaced by the IDC values later.

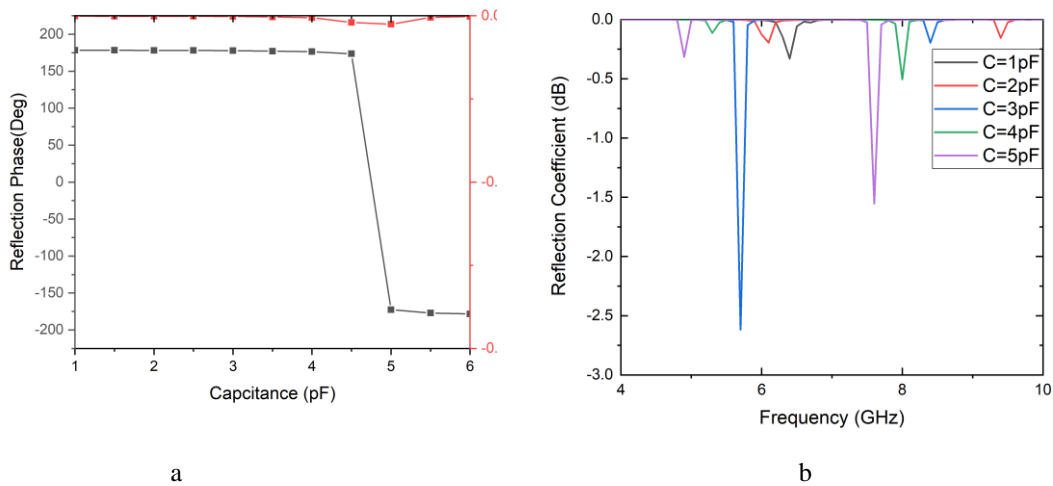


Figure 54. Phase and Reflection profile of the proposed unit cell

As can be seen from Fig 54(a), a large phase variation is achieved for the unit cell when the series capacitance varies between 4pF to 6pF. Hence, these capacitances range will be exploited in the next steps.

5.6.4 Super Cell Configuration

As established in the chapter 4, in order to have an anomalous reflector, we need to make a super cell which is nothing, but the combination of the unit cell shown in Fig.52. Configuration of the super cell is made to enhance the power coupling efficiency of the reflector in an anomalous direction by suppressing the parasitic reflection from the IRS. In this case, a supercell composed of 10-unit cells has been formed. When dimension of the super cell falls between λ_0 and $2\lambda_0$, three diffraction orders are expected [94]. The dimension of the supercell is $D=72.5 \text{ mm} \sim 1.2\lambda_0$, so at normal incident expected diffraction orders are $m=0, \pm 1$.

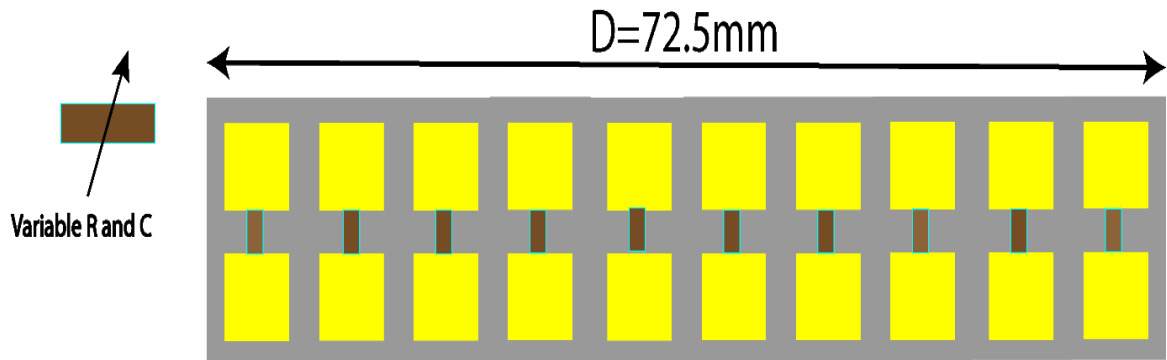


Figure 55 Super Cell consisting of 10-unit cell

Values of the capacitances have changed in a linear fashion between 4 pF to 6 pF according to the phase variations shown in Fig. 54(a).

Simulations are done in HFSS for the TE polarized normally incident plane using Floquet port and periodic boundary conditions. Optimization on the capacitance values is being asked in order to enhance the reflection towards $m=1$ diffraction order.

5.6.5 Interdigital Capacitor

Alongside the optimization of the supercell response, an IDC has been designed to verify the impact of HfZrO tunability: the layout of an IDC should be highly dependent on the permittivity value of the dielectric in between its fingers. Therefore, the idea is to exploit the bias-dependent ferroelectric effect of the HfZrO shown in Table 5 for this purpose. Fig. 56 shows the design of the IDC with 6 fingers. Same substrate values for Si and HfZrO have been chosen here as well.

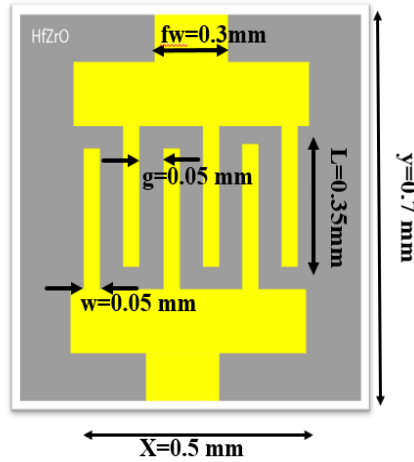


Figure 56. Design parameters of IDC

Microstrip fed two-port IDC design was simulated. Lumped element approximation is valid in this case as the size of the IDC is small. The capacitance of the IDC is directly proportional to the number of fingers and length of the fingers. Interdigital gap can be utilized to fine tune the capacitance values as per requirement of the supercell.

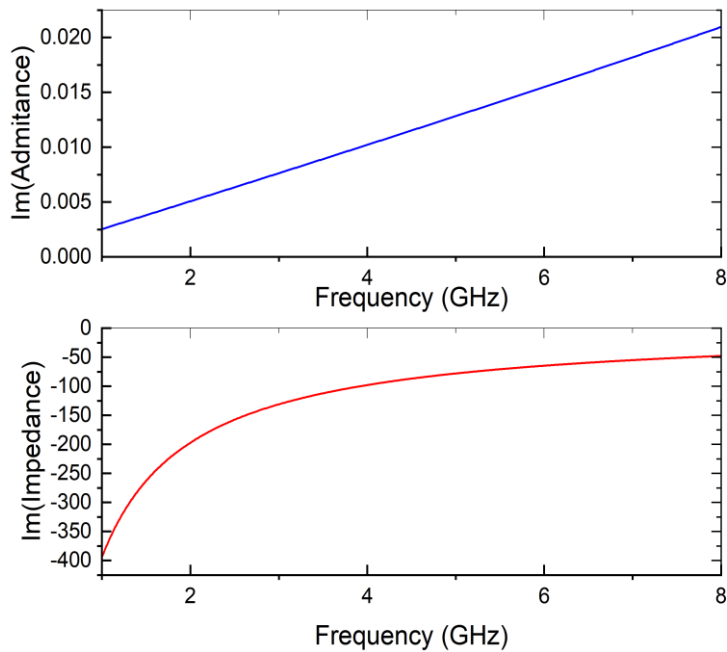


Figure 57 IDC results without biasing of HfZrO

Fig 57 shows the simulated IDC results, the capacitance value of the IDC shown in Fig. 56 is around 0.4 pF in this case for 5GHz frequency. This value needs to be tuned in the future activity to fit the 4-6 pF range needed

to enter the most sensitive region of the supercell reflector behaviour: by changing the HfZrO biasing according to the Table 5, the envisaged IDC tunability should be guaranteed.

5.7 Conclusion and Future Work

An angularly stable super wideband metasurface is presented in the chapter. The proposed metasurface operates in 11 - 35GHz with more than 60% conversion efficiency throughout. The efficiency of the proposed surface reaches more than 90% for some frequencies within the operational band. The metasurface can convert an X-polarized incident wave into Y-polarized wave and vice versa. Further, performance under oblique incident waves is also studied and results show that the proposed design operates well up to 40° of oblique incidence. The proposed metasurface is a potential solution for polarization conversion for super wideband applications.

In the second section of the chapter, a very promising design methodology for a reconfigurable intelligent reflector has been presented by utilizing the thin layer of a new material (HfZrO). The continuous tunability of the surface will be exploited by benefitting from the voltage dependent intrinsic properties of the HfZrO. The proposed anomalous reflector is a globally tuned IRS.

The IRS is still in the optimization phase however results so far obtained are indicating positive prospect of the metasurface.

For the tunability of the surface an FPGA based approach is under consideration to bias the HfZrO between 0 to 5 volts in a continuous fashion.

In future, the study of IRS will be continued till its completion. Furthermore, after the anomalous reflection intelligent beam steering scenarios will be considered.

CHAPTER 6

Summary of the Thesis.

This thesis can be categorized as a study of the various wireless systems. Complete analysis and modelling of the different aspects of such systems have been considered and discussed in detail. Thesis aims to be in accordance with the current research trends and practices of the relevant fields. Special attention has been paid to propose applications-oriented solutions keeping in mind the future needs. Thesis can be classified into two major sections. First section of the thesis has been dedicated towards the near-field wireless systems and the second section of the thesis considers the far-field systems.

In the first section, the thesis takes into account the simultaneous wireless information and power transfer (SWIPT) application in a transportation scenario, with special consideration of the near-field wireless power transfer (WPT) system and its coexistence with neighbouring subsystems. Three coil-based transmitters have been realised to work at different frequencies. WPT link was optimized for the transfer of power at 27MHz while other two subsystems or sub links have been created for communication and test purposes at 4MHz and 6MHz respectively.

To ensure the isolation of systems performance geometrical aspects, as well as trapping filters are considered to virtually isolate the WPT system from the rest of the system without losing the requisite criteria for the WPT. As a peculiarity of the work, the system is considered as a whole, from the biasing of the inverter on the transmitting side to the receiving loop load.

Class E power amplifier has been adopted to power the transmitter with high efficiency. Furthermore, the study also highlights aspects of near-field SWIPT to a moving transmitter that makes the problem at hand more complex. It has been shown that although the proposed system is based on the resonance the whole system can be optimized to provide the stable power at different misalignments.

In the second part of the thesis, a comprehensive approach has been adopted to model and design the metamaterial-based systems. Two distinctive studies have been done to exploit the metasurface in two applications.

Firstly, a resonant meta surface has been designed and optimized to interconvert the linear polarizations with high efficiency. The proposed metasurface exploits two ring resonator that are placed in such a way that they give a super wide band response for different incident angles varying from 0° to 40° with polarization conversion efficiency always greater than 60%.

Second metasurface based activity, presented in the thesis, is related to the IRS. A novel approach has been proposed to design a square patched globally reconfigurable metasurface which can reflect the incident wave to the anomalous direction. The direction of the reflected field has been proposed to be controlled globally by introducing a thin layer of the novel material HfZrO which has the ability to change the permittivity depending upon the external low voltage biasing conditions. A super cell approach has been adopted and HfZrO based IDC has been designed to be paced between the patches in a super cell to provide the impedance change. The study is under progress and once completed it will be a novel solution for the beam steering applications.

The research work has been done under two different collaborations from Rete Ferroviaria Italiana (RFI) and H2020 NanoEH project. The thesis has resulted into 4 publications and would further result into two more publication coming from the IRS activity in the near future.

References

- [1] F. Benassi, D. Masotti and A. Costanzo, "Engineered and miniaturized 13.56 MHz omni-directional WPT system for medical applications," *2019 IEEE International Conference on RFID Technology and Applications (RFID-TA)*, 2019, pp. 306-309, doi: 10.1109/RFID-TA.2019.8892169.
- [2] T. Campi, S. Cruciani, F. Maradei and M. Feliziani, "Innovative Wireless Charging System for Implantable Capsule Robots," in *IEEE Transactions on Electromagnetic Compatibility*, vol. 63, no. 5, pp. 1726-1734, Oct. 2021, doi: 10.1109/TEM.2021.3078846.
- [3] T. Campi, S. Cruciani, F. Maradei, A. Montalto, F. Musumeci and M. Feliziani, "Centralized High Power Supply System for Implanted Medical Devices Using Wireless Power Transfer Technology," in *IEEE Transactions on Medical Robotics and Bionics*, vol. 3, no. 4, pp. 992-1001, Nov. 2021, doi: 10.1109/TMRB.2021.3123404.
- [4] Z. Ye, M. Yang and P. -Y. Chen, "Multi-Band Parity-Time-Symmetric Wireless Power Transfer Systems for ISM-Band Bio-Implantable Applications," in *IEEE Journal of Electromagnetics, RF and Microwaves in Medicine and Biology*, doi: 10.1109/JERM.2021.3120621.
- [5] S. G. Jang, J. Kim, J. Lee, J. S. Kim, D. Hwan Kim and S. M. Park, "Wireless Power Transfer Based Implantable Neurostimulator," *2020 IEEE Wireless Power Transfer Conference (WPTC)*, 2020, pp. 365-368, doi: 10.1109/WPTC48563.2020.9295553.
- [6] M. Manoufali, K. Bialkowski, B. J. Mohammed, P. C. Mills and A. Abbosh, "Near-Field Inductive-Coupling Link to Power a Three-Dimensional Millimeter-Size Antenna for Brain Implantable Medical Devices," in *IEEE Transactions on Biomedical Engineering*, vol. 65, no. 1, pp. 4-14, Jan. 2018, doi: 10.1109/TBME.2017.2778729.
- [7] Q. Wang, W. Che, M. Mongiardo and G. Monti, "Wireless Power Transfer System With High Misalignment Tolerance for Bio-Medical Implants," in *IEEE Transactions on Circuits and Systems II: Express Briefs*, vol. 67, no. 12, pp. 3023-3027, Dec. 2020, doi: 10.1109/TCSII.2020.2985056.
- [8] T. Shaw, G. Samanta and D. Mitra, "Efficient Wireless Power Transfer System for Implantable Medical Devices Using Circular Polarized Antennas," in *IEEE Transactions on Antennas and Propagation*, vol. 69, no. 7, pp. 4109-4122, July 2021, doi: 10.1109/TAP.2020.3044636.
- [9] M. Wang *et al.*, "Broadband Implantable Antenna for Wireless Power Transfer in Cardiac Pacemaker Applications," in *IEEE Journal of Electromagnetics, RF and Microwaves in Medicine and Biology*, vol. 5, no. 1, pp. 2-8, March 2021, doi: 10.1109/JERM.2020.2999205

- [10] Khan, S.R.; Pavuluri, S.K.; Cummins, G.; Desmulliez, M.P.Y. Wireless Power Transfer Techniques for Implantable Medical Devices: A Review. *Sensors* **2020**, *20*, 3487. <https://doi.org/10.3390/s20123487>
- [11] N. Fu, J. Deng, Z. Wang, W. Wang and S. Wang, "A Hybrid Mode Control Strategy for LCC–LCC- Compensated WPT System With Wide ZVS Operation," in *IEEE Transactions on Power Electronics*, vol. 37, no. 2, pp. 2449-2460, Feb. 2022, doi: 10.1109/TPEL.2021.3108637.
- [12] H. Wang, U. Pratik, A. Jovicic, N. Hasan and Z. Pantic, "Dynamic Wireless Charging of Medium Power and Speed Electric Vehicles," in *IEEE Transactions on Vehicular Technology*, vol. 70, no. 12, pp. 12552-12566, Dec. 2021, doi: 10.1109/TVT.2021.3122366.
- [13] F. Wen, X. Chu, Q. Li, W. Zhao, X. Zhu and Y. Wu, "Receiver Localization Strategy of Wireless Charging System Based on Mutual Inductance Disturbance," in *IEEE Transactions on Applied Superconductivity*, vol. 31, no. 8, pp. 1-4, Nov. 2021, Art no. 0600604, doi: 10.1109/TASC.2021.3091121.
- [14] N. Khan, H. Matsumoto and O. Trescases, "Wireless Electric Vehicle Charger With Electromagnetic Coil-Based Position Correction Using Impedance and Resonant Frequency Detection," in *IEEE Transactions on Power Electronics*, vol. 35, no. 8, pp. 7873-7883, Aug. 2020, doi: 10.1109/TPEL.2020.2965476.
- [15] S. Ann and B. K. Lee, "Analysis of Impedance Tuning Control and Synchronous Switching Technique for a Semibridgeless Active Rectifier in Inductive Power Transfer Systems for Electric Vehicles," in *IEEE Transactions on Power Electronics*, vol. 36, no. 8, pp. 8786-8798, Aug. 2021, doi: 10.1109/TPEL.2021.3049546.
- [16] H. Chen *et al.*, "Modular Four-Channel 50 kW WPT System With Decoupled Coil Design for Fast EV Charging," in *IEEE Access*, vol. 9, pp. 136083-136093, 2021, doi: 10.1109/ACCESS.2021.3116696.
- [17] A. U. Ibrahim, W. Zhong and M. D. Xu, "A 50-kW Three-Channel Wireless Power Transfer System With Low Stray Magnetic Field," in *IEEE Transactions on Power Electronics*, vol. 36, no. 9, pp. 9941-9954, Sept. 2021, doi: 10.1109/TPEL.2021.3064373.
- [18] H. Gu and H. Choi, "Analysis of Wireless Power Transmission Characteristics for High-Efficiency Resonant Coils," in *IEEE Transactions on Applied Superconductivity*, vol. 30, no. 4, pp. 1-4, June 2020, Art no. 5400304, doi: 10.1109/TASC.2020.2966424.
- [19] Y. Chen, H. Zhang, C. -S. Shin, C. -H. Jo, S. -J. Park and D. -H. Kim, "An Efficiency Optimization-Based Asymmetric Tuning Method of Double-Sided LCC

Compensated WPT System for Electric Vehicles," in *IEEE Transactions on Power Electronics*, vol. 35, no. 11, pp. 11475-11487, Nov. 2020, doi: 10.1109/TPEL.2020.2984712.

[20] J. Li, F. Yin and L. Wang, "Transmission efficiency of different shielding structures in wireless power transfer systems for electric vehicles," in *CSEE Journal of Power and Energy Systems*, vol. 7, no. 6, pp. 1247-1255, Nov. 2021, doi: 10.17775/CSEEJPES.2019.00500.

[21] M. Xiong, X. Wei, Y. Huang, Z. Luo and H. Dai, "Research on Novel Flexible High-Saturation Nanocrystalline Cores for Wireless Charging Systems of Electric Vehicles," in *IEEE Transactions on Industrial Electronics*, vol. 68, no. 9, pp. 8310-8320, Sept. 2021, doi: 10.1109/TIE.2020.3016259.

[22] M. A. Tawfik *et al.*, "On Using CNTFs-Based Wires for High Frequency Wireless Power Transfer Charging Systems," in *IEEE Transactions on Nanotechnology*, vol. 20, pp. 784-793, 2021, doi: 10.1109/TNANO.2021.3119695.

[23] S. Li, S. Lu and C. C. Mi, "Revolution of Electric Vehicle Charging Technologies Accelerated by Wide Bandgap Devices," in *Proceedings of the IEEE*, vol. 109, no. 6, pp. 985-1003, June 2021, doi: 10.1109/JPROC.2021.3071977.

[24] T. D. Ponnimbaduge Perera, S. Panic, D. N. K. Jayakody, P. Muthu Chidambaranathan and J. Li, "A WPT-Enabled UAV-Assisted Condition Monitoring Scheme for Wireless Sensor Networks," in *IEEE Transactions on Intelligent Transportation Systems*, vol. 22, no. 8, pp. 5112-5126, Aug. 2021, doi: 10.1109/TITS.2020.3018493.

[25] C. Guo and D. Zhao, "Joint Charging, Routing, and Power Allocations in Rechargeable Wireless Sensor Networks," *2021 International Wireless Communications and Mobile Computing (IWCMC)*, 2021, pp. 1436-1441, doi: 10.1109/IWCMC51323.2021.9498610.

[26] A. Singh and M. J. Nene, "Model for Self-Energizing Wireless Sensor Network," *2019 IEEE 5th International Conference for Convergence in Technology (I2CT)*, 2019, pp. 1-6, doi: 10.1109/I2CT45611.2019.9033812.

[27] S. -W. Dong *et al.*, "Hybrid Mode Wireless Power Transfer for Wireless Sensor Network," *2019 IEEE Wireless Power Transfer Conference (WPTC)*, 2019, pp. 561-564, doi: 10.1109/WPTC45513.2019.9055665.S

[28] A. Litvinenko, R. Kusnins, A. Aboltins, J. Eidaks, D. Laksis and J. Sadovksis, "About Simultaneous Information and Power Transfer in WSN using Frequency Modulation," *2020 IEEE 8th Workshop on Advances in Information, Electronic and Electrical Engineering (AIEEE)*, 2021, pp. 1-6, doi: 10.1109/AIEEE51419.2021.9435778.

[29] M. Poveda-García, J. Oliva-Sánchez, R. Sanchez-Iborra, D. Cañete-Rebenaque and J. L. Gomez-Tornero, "Dynamic Wireless Power Transfer for Cost-Effective

Wireless Sensor Networks Using Frequency-Scanned Beaming," in *IEEE Access*, vol. 7, pp. 8081-8094, 2019, doi: 10.1109/ACCESS.2018.2886448.

[30] Z. Zhang and B. Zhang, "Omnidirectional and Efficient Wireless Power Transfer System for Logistic Robots," in *IEEE Access*, vol. 8, pp. 13683-13693, 2020, doi: 10.1109/ACCESS.2020.2966225.

[31] A. Sarin and A. -T. Avestruz, "Code Division Multiple Access Wireless Power Transfer for Energy Sharing in Heterogenous Robot Swarms," in *IEEE Access*, vol. 8, pp. 132121-132133, 2020, doi: 10.1109/ACCESS.2020.3010202.

[32] D. -Z. Kim *et al.*, "High efficient power receiver IC with load modulator for wireless resonant power transfer," *2012 42nd European Microwave Conference*, 2012, pp. 416-419, doi: 10.23919/EuMC.2012.6459428.

[33] Merz, Christian, Daniel Gückelhorn, and Cem Som. "Circuit and Antenna Design of a Simultaneous Wireless Power Transfer and Near Field Communication System."

[34] P. Han, X. Wang, J. Zhang and Y. Ji, "Magnetic Coupling Resonant Simultaneous Wireless Power and Information Transfer System with Switched Relay Resonators," *2021 IEEE Asia-Pacific Microwave Conference (APMC)*, 2021, pp. 449-451, doi: 10.1109/APMC52720.2021.9661643.

[35] M. Ishii, K. Yamanaka and M. Sasaki, "Multiple FSK Data and Power Transmission System using Magnetic Resonance Wireless Power Transfer," *2019 IEEE Wireless Power Transfer Conference (WPTC)*, 2019, pp. 208-211, doi: 10.1109/WPTC45513.2019.9055549.

[36] K. W. Choi *et al.*, "Simultaneous Wireless Information and Power Transfer (SWIPT) for Internet of Things: Novel Receiver Design and Experimental Validation," in *IEEE Internet of Things Journal*, vol. 7, no. 4, pp. 2996-3012, April 2020, doi: 10.1109/JIOT.2020.2964302.

[37] T. Ikeuchi and Y. Kawahara, "Peak to Average Power Ratio Based Signal Detection for Frequency Shift Multitone SWIPT System," in *IEEE Access*, vol. 9, pp. 4158-4172, 2021, doi: 10.1109/ACCESS.2020.3048193.

[38] A. Barakat, R. K. Pokharel, S. Alshhawy, K. Yoshitomi and S. Kawasaki, "High Isolation Simultaneous Wireless Power and Information Transfer System Using Coexisting DGS resonators and Figure-8 Inductors," *2020 IEEE/MTT-S International Microwave Symposium (IMS)*, 2020, pp. 1172-1175, doi: 10.1109/IMS30576.2020.9223866.

[39] R. Fischbacher *et al.*, "EC Model for WPT and NFC Systems Interoperability Analysis," *2021 IEEE Radio and Wireless Symposium (RWS)*, 2021, pp. 112-115, doi: 10.1109/RWS50353.2021.9360370.

- [40] G. Paolini, M. Feliciani, D. Masotti and A. Costanzo, "Toward an Energy-Autonomous Wearable System for Human Breath Detection," *2020 IEEE MTT-S International Microwave Biomedical Conference (IMBioC)*, 2020, pp. 1-3, doi: 10.1109/IMBioC47321.2020.9385027.
- [41] A. Iqbal, M. Al-Hasan, I. B. Mabrouk, A. Basir, M. Nedil and H. Yoo, "Biotelemetry and Wireless Powering of Biomedical Implants Using a Rectifier Integrated Self-Diplexing Implantable Antenna," in *IEEE Transactions on Microwave Theory and Techniques*, vol. 69, no. 7, pp. 3438-3451, July 2021, doi: 10.1109/TMTT.2021.3065560.
- [42] T. Wang, Q. Xu, W. Jia, Z. -H. Mao, H. Tang and M. Sun, "Dual-Functional Wireless Power Transfer and Data Communication Design for Micromedical Implants," in *IEEE Journal of Emerging and Selected Topics in Power Electronics*, vol. 9, no. 5, pp. 6259-6271, Oct. 2021, doi: 10.1109/JESTPE.2021.3049787.
- [43] D. Rodriguez, M. A. Saed and C. Li, "A WPT/NFC-Based Sensing Approach for Beverage Freshness Detection Using Supervised Machine Learning," in *IEEE Sensors Journal*, vol. 21, no. 1, pp. 733-742, 1 Jan.1, 2021, doi: 10.1109/JSEN.2020.3013506.
- [44] D. Ye, Y. Wang, Y. Xiang, L. Lyu, H. Min and C.. -J. R. Shi, "A Wireless Power and Data Transfer Receiver Achieving 75.4% Effective Power Conversion Efficiency and Supporting 0.1% Modulation Depth for ASK Demodulation," in *IEEE Journal of Solid-State Circuits*, vol. 55, no. 5, pp. 1386-1400, May 2020, doi: 10.1109/JSSC.2019.2943871.
- [45] D. Pires, D. Belo, M. Jordão, P. Pinho and N. B. d. Carvalho, "3D Antenna Array for SWIPT Sensing with WPT Capabilities," *2020 14th European Conference on Antennas and Propagation (EuCAP)*, 2020, pp. 1-4, doi: 10.23919/EuCAP48036.2020.9135504.
- [46] Van Schuylenbergh, Koenraad, and Robert Puers. *Inductive powering: basic theory and application to biomedical systems*. Springer Science & Business Media, 2009
- [47] Z. Zhang, H. Pang, A. Georgiadis and C. Cecati, "Wireless Power Transfer—An Overview," in *IEEE Transactions on Industrial Electronics*, vol. 66, no. 2, pp. 1044-1058, Feb. 2019, doi: 10.1109/TIE.2018.2835378.
- [48] Y. H. Sohn, B. H. Choi, E. S. Lee, G. C. Lim, G. Cho and C. T. Rim, "General Unified Analyses of Two-Capacitor Inductive Power Transfer Systems: Equivalence of Current-Source SS and SP Compensations," in *IEEE Transactions on Power Electronics*, vol. 30, no. 11, pp. 6030-6045, Nov. 2015, doi: 10.1109/TPEL.2015.2409734.
- [49] Marian K. Kazimierczuk "RF Power Amplifiers" November 2014 doI:10.1002/978111884437

- [50] S. Aldhafer, D. C. Yates and P. D. Mitcheson, "Load-Independent Class E/EF Inverters and Rectifiers for MHz-Switching Applications," in *IEEE Transactions on Power Electronics*, vol. 33, no. 10, pp. 8270-8287, Oct. 2018, doi: 10.1109/TPEL.2018.2813760
- [51] E. Bahat-Treidel, "GaN Based HEMTs for High Voltage Operation. Design, Technology and Characterization", PhD thesis, Technische Universität Berlin, 2012. doi:10.14279/depositonce-3203
- [52] Y. Hongyu, *Gallium Nitride Power Devices*, 1st ed. Pan Stanford Publishing, 2017, isbn: 9789814774093
- [53] D.C. Marian K. Kazimierczuk, "Resonant Power Converters", 2nd Edition, Wiley, 2011
- [54] G. Bouattour, Z. Hu, H. B. Jmeaa Derbel and O. Kanoun, "Smart Multi-coil Inductive Power Transmission with IoT Based Visualization," *2020 IEEE 6th World Forum on Internet of Things (WF-IoT)*, 2020, pp. 1-6, doi: 10.1109/WF-IoT48130.2020.9221284.
- [55] S. K. Abed, "European Rail Traffic Management System - An overview," 2010 1st International Conference on Energy, Power and Control (EPC-IQ), 2010, pp. 173-180.
- [56] J. B. Pendry, A. J. Holden, D. J. Robbins and W. J. Stewart, "Magnetism from conductors and enhanced nonlinear phenomena," in *IEEE Transactions on Microwave Theory and Techniques*, vol. 47, no. 11, pp. 2075-2084, Nov. 1999, doi: 10.1109/22.798002.
- [57] Shelby, Richard A., David R. Smith, and Seldon Schultz. "Experimental verification of a negative index of refraction." *science* 292.5514 (2001): 77-79.
- [58] Soukoulis, Costas M., and Martin Wegener. "Past achievements and future challenges in the development of three-dimensional photonic metamaterials." *Nature photonics* 5.9 (2011): 523-530
- [59] Qu, Che, et al. "Tailor the functionalities of metasurfaces based on a complete phase diagram." *Physical review letters* 115.23 (2015): 235503.
- [60] Lei Wang, Shijun Ge, Wei Hu, Makoto Nakajima, and Yanqing Lu, "Graphene-assisted high-efficiency liquid crystal tunable terahertz metamaterial absorber," *Opt. Express* 25, 23873-23879 (2017)
- [61] Tsilipakos, Odysseas, et al. "Toward intelligent metasurfaces: the progress from globally tunable metasurfaces to software-defined metasurfaces with an embedded network of controllers." *Advanced Optical Materials* 8.17 (2020): 2000783.
- [62] Xu, He-Xiu, et al. "Dynamical control on helicity of electromagnetic waves by tuneable metasurfaces." *Scientific reports* 6.1 (2016): 1-10.

- [63] Tao, Zui, et al. "Reconfigurable conversions of reflection, transmission, and polarization states using active metasurface." *Applied Physics Letters* 110.12 (2017): 121901.
- [64] A. Li, S. Kim, Y. Luo, Y. Li, J. Long and D. F. Sievenpiper, "High-Power Transistor-Based Tunable and Switchable Metasurface Absorber," in *IEEE Transactions on Microwave Theory and Techniques*, vol. 65, no. 8, pp. 2810-2818, Aug. 2017, doi: 10.1109/TMTT.2017.2681650.
- [65] Chen, HT., Padilla, W., Zide, J. et al. Active terahertz metamaterial devices. *Nature* 444, 597–600 (2006). <https://doi.org/10.1038/nature05343>
- [66] Chen, X., Tian, Z., Lu, Y., Xu, Y., Zhang, X., Ouyang, C., Gu, J., Han, J., Zhang, W., Electrically Tunable Perfect Terahertz Absorber Based on a Graphene Salisbury Screen Hybrid Metasurface. *Adv. Optical Mater.* 2020, 8, 1900660. <https://doi.org/10.1002/adom.201900660>
- [67] Zhang, Fuli, et al. "Electrically controllable fishnet metamaterial based on nematic liquid crystal." *Optics express* 19.2 (2011): 1563-1568.
- [68] Kossifos, Kypros M., et al. "An optically-programmable absorbing metasurface." 2018 IEEE International Symposium on Circuits and Systems (ISCAS). IEEE, 2018.
- [69] Xu, He-Xiu, et al. "Tunable microwave metasurfaces for high-performance operations: dispersion compensation and dynamical switch." *Scientific reports* 6.1 (2016): 1-10.
- [70] Yang, Huanhuan, et al. "A programmable metasurface with dynamic polarization, scattering and focusing control." *Scientific reports* 6.1 (2016): 1-11.
- [71] Li, L., Jun Cui, T., Ji, W. et al. Electromagnetic reprogrammable coding-metasurface holograms. *Nat Commun* 8, 197 (2017). <https://doi.org/10.1038/s41467-017-00164-9>
- [72] K. M. Kossifos et al., "Toward the Realization of a Programmable Metasurface Absorber Enabled by Custom Integrated Circuit Technology," in *IEEE Access*, vol. 8, pp. 92986-92998, 2020, doi: 10.1109/ACCESS.2020.2994469.
- [73] Jiang, Huan, Ying Cui, and Yongyuan Jiang. "Two-dimensional tunable polarization-dependent absorptions for binary and ternary coding." *Optical Materials Express* 10.3 (2020): 787-795.
- [74] Wan, Xiang, et al. "Field-programmable beam reconfiguring based on digitally-controlled coding metasurface." *Scientific reports* 6.1 (2016): 1-8.

- [75] Huang, Chongwen, et al. "Reconfigurable intelligent surfaces for energy efficiency in wireless communication." *IEEE Transactions on Wireless Communications* 18.8 (2019): 4157-4170.
- [76] M. Di Renzo et al., "Smart Radio Environments Empowered by Reconfigurable Intelligent Surfaces: How It Works, State of Research, and The Road Ahead," in *IEEE Journal on Selected Areas in Communications*, vol. 38, no. 11, pp. 2450-2525, Nov. 2020, doi: 10.1109/JSAC.2020.3007211.
- [77] M. A. ElMossallamy, H. Zhang, L. Song, K. G. Seddik, Z. Han and G. Y. Li, "Reconfigurable Intelligent Surfaces for Wireless Communications: Principles, Challenges, and Opportunities," in *IEEE Transactions on Cognitive Communications and Networking*, vol. 6, no. 3, pp. 990-1002, Sept. 2020, doi: 10.1109/TCCN.2020.2992604.
- [78] C. Molero et al., "Metamaterial-Based Reconfigurable Intelligent Surface: 3D Meta-Atoms Controlled by Graphene Structures," in *IEEE Communications Magazine*, vol. 59, no. 6, pp. 42-48, June 2021, doi: 10.1109/MCOM.001.2001161.
- [79] A. Elzanaty, A. Guerra, F. Guidi and M. -S. Alouini, "Reconfigurable Intelligent Surfaces for Localization: Position and Orientation Error Bounds," in *IEEE Transactions on Signal Processing*, vol. 69, pp. 5386-5402, 2021, doi: 10.1109/TSP.2021.3101644.
- [80] S. Kisseleff, W. A. Martins, H. Al-Hraishawi, S. Chatzinotas and B. Ottersten, "Reconfigurable Intelligent Surfaces for Smart Cities: Research Challenges and Opportunities," in *IEEE Open Journal of the Communications Society*, vol. 1, pp. 1781-1797, 2020, doi: 10.1109/OJCOMS.2020.3036839.
- [81] K. Yu, X. Yu and J. Cai, "UAVs Assisted Intelligent Reflecting Surfaces SWIPT System With Statistical CSI," in *IEEE Journal of Selected Topics in Signal Processing*, vol. 15, no. 5, pp. 1095-1109, Aug. 2021, doi: 10.1109/JSTSP.2021.3096025.
- [82] S. Fernández, F. Gregorio, B. K. Chalise and J. Cousseau, "Wireless Information and power transfer assisted by reconfigurable intelligent surfaces : Invited Paper," 2021 Argentine Conference on Electronics (CAE), 2021, pp. 73-77, doi: 10.1109/CAE51562.2021.9397565.
- [83] Faenzi, Marco, et al. "Metasurface antennas: new models, applications and realizations." *Scientific reports* 9.1 (2019): 1-14.
- [84] A. Shahvarpour, A. A. Melcon and C. Caloz, "Anisotropic meta-substrate conical-beam leaky-wave antenna," 2010 Asia-Pacific Microwave Conference, 2010, pp. 299-302.
- [85] Caiazzo, Maci and Engheta, "A metamaterial surface for compact cavity resonators," in *IEEE Antennas and Wireless Propagation Letters*, vol. 3, pp. 261-264, 2004, doi: 10.1109/LAWP.2004.836576.
- [86] Li, Lianlin, et al. "Electromagnetic reprogrammable coding-metasurface holograms." *Nature communications* 8.1 (2017): 1-7.

- [87] Ye, Yuqian, and Sailing He. "90° polarization rotator using a bilayered chiral metamaterial with giant optical activity." *Applied Physics Letters* 96.20 (2010): 203501.
- [88] N. Amitay and A. A. M. Saleh, "Broad-band wide-angle quasi-optical polarization rotators," in *IEEE Transactions on Antennas and Propagation*, vol. 31, no. 1, pp. 73-76, January 1983, doi: 10.1109/TAP.1983.1143017.
- [89] Plum, E., et al. "Metamaterial with negative index due to chirality." *Physical Review B* 79.3 (2009): 035407.
- [90] Pendry, John B., David Schurig, and David R. Smith. "Controlling electromagnetic fields." *science* 312.5781 (2006): 1780-1782.
- [91] Schurig, David, et al. "Metamaterial electromagnetic cloak at microwave frequencies." *Science* 314.5801 (2006): 977-980.
- [92] Howell, John C., and J. Benjamin Howell. "Simple, broadband, optical spatial cloaking of very large objects." *arXiv preprint arXiv:1306.0863* (2013).
- [93] J. Lee et al., "Giant nonlinear response from plasmonic metasurfaces coupled to intersubband transitions," 2014 Conference on Lasers and Electro-Optics (CLEO) - Laser Science to Photonic Applications, 2014, pp. 1-2.
- [94] Liu, Fu, et al. "Intelligent metasurfaces with continuously tunable local surface impedance for multiple reconfigurable functions." *Physical Review Applied* 11.4 (2019): 044024
- [95] Katsarakis, N., et al. "Electric coupling to the magnetic resonance of split ring resonators." *Applied physics letters* 84.15 (2004): 2943-2945.
- [96] Khan, M. Ismail, and Farooq A. Tahir. "An angularly stable dual-broadband anisotropic cross polarization conversion metasurface." *Journal of Applied Physics* 122.5 (2017): 053103.
- [97] Lin, Baoqin, et al. "Dual-band high-efficiency polarization converter using an anisotropic metasurface." *Journal of Applied Physics* 119.18 (2016): 183103
- [98] M. Murtaza, A. Rashid, T. Ullah, F. A. Tahir and S. A. A. Zaidi, "An Angularly Stable Broadband Cross-Polarization Conversion Metasurface," 2019 13th European Conference on Antennas and Propagation (EuCAP), 2019, pp. 1-3.
- [99] C. Kong, Z. Li and Z. Wu, "Ultra-wideband polarization conversion metasurface," 2016 11th International Symposium on Antennas, Propagation and EM Theory (ISAPE), 2016, pp. 210-212, doi: 10.1109/ISAPE.2016.7833918.
- [100] Chen, Hongya, et al. "Ultra-wideband polarization conversion metasurfaces based on multiple plasmon resonances." *Journal of Applied Physics* 115.15 (2014): 154504.
- [101] Khan, M. Ismail, and Farooq A. Tahir. "A broadband cross-polarization conversion anisotropic metasurface based on multiple plasmon resonances." *Chinese Physics B* 27.1 (2018): 014101.

- [102] M. Mustafa and F. A. Tahir, "A Broadband Metasurface for Cross Polarization Conversion Applications," 2019 13th European Conference on Antennas and Propagation (EuCAP), 2019, pp. 1-2.
- [103] R. Izhar, Meraj-E-Mustafa, M. S. Wahidi and F. A. Tahir, "An Anisotropic Dual-Broadband CPC Metasurface," 2019 International Conference on Microwave and Millimeter Wave Technology (ICMMT), 2019, pp. 1-2, doi: 10.1109/ICMMT45702.2019.8992081.
- [104] Meraj-E-Mustafa, R. Izhar, M. S. Wahidi, F. A. Tahir and Q. H. Abbasi, "A Broadband Polarization Rotator Metasurface," 2019 International Conference on Microwave and Millimeter Wave Technology (ICMMT), 2019, pp. 1-2, doi: 10.1109/ICMMT45702.2019.8992370.
- [105] M. Aldrigo et al., "Microwave applications of zirconium-doped hafnium oxide ferroelectrics: from nanoscale calculations up to experimental results," 2020 IEEE/MTT-S International Microwave Symposium (IMS), 2020, pp. 520-523, doi: 10.1109/IMS30576.2020.9224016.
- [106] S. Agarwal, G. Murtaza, A. Costanzo and D. Masotti, "A Super Wideband Angularly Stable Metasurface for Cross Polarization Conversion Applications," 2021 International Microwave and RF Conference (IMaRC), 2021.